UNIVERSITY OF GRONINGEN

The Anomalous Hall Effect for Magnons

by

Walewein Noordam, S2389525

in the
Faculty of Mathematics and Natural Sciences
University of Groningen

July 2016

UNIVERSITY OF GRONINGEN

Abstract

Faculty of Mathematics and Natural Sciences
University of Groningen

by Walewein Noordam, S2389525

An investigation on magnon transport is done on 100 nm thick YIG with platinum wires, $\sim 7\,nm$ thick. A comparison is done with 200 nm thick YIG for measurements of which the result is already known [1] and the Anomalous Hall Effect for magnons itself is being investigated. The SMR of 100 nm thick YIG gives the same magnitude and sign as for 200 nm YIG. The local SSE voltage of the second harmonic shows a same sign and magnitude when compared with 200 nm YIG. The in plane measurements show the same sign and the first harmonic in plane measurements have a similar magnitude when compared to 200 nm thick YIG. The magnitude of the second harmonic in plane measurements is however twice as small. The out of plane measurements show that one of the signals is an artifact from the measurement setup due to the SW model. The hypotheses drawn for the AHE for magnons expect a 2-fold and 3-fold signal should be seen in the second harmonic and first harmonic respectively for out of plane measurements. These signals are however not found, which could be due to the reason that the AHE for magnons is a bulk effect or that the device geometry is not suitable.

...

Contents

Chapter 1

Introduction

1.1 Technological Singularity

In the last few decades amazing progress has been made on advancing the technology of man. One quintessential example is Moore´s Law which states that the amount of transistors on an integrated circuit will double every two years. This trend has been observed over the last few decades, but one might imagine that it´s eventually not possible to go any further. That there must be some limit after which no transistor can be made anymore. This limit could then be called a technological singularity, this limit has been noted by John von Neumann in the 1950s, ¨An essential singularity in the history of the race, on the ever accelerating progress of technology, beyond which human affairs, as we know them, could not continue¨[2].

With the advancement of spin-integrated electronics, or spintronics, it´s been possible to keep making the transistors smaller by making use of the electron spin, a result from quantum mechanics. This translates to the fact that it is still possible to match the description of Moore´s Law. However, to effectively develop integrated circuits based on spintronics is important to know all the mechanism that are present when using this technology. And that is where this bachelor research enters the picture.

1.2 Magnons

Now what is this magnon and why is it studied, besides shear interest of finding out all there is to know. To explain that we start off with a ferromagnet. When this ferromagnet is in its ground state, the spins are all pointing in the same direction, see figure 1.1(a). When some energy is added to this ferromagnet, it will go into an excited state, where

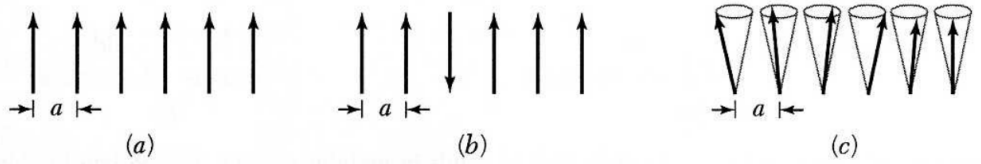

FIGURE 1.1: (a) A ferromagnet in its ground state, all the spins are aligned in the same direction. (b) A ferromagnet in a high energy excited state, one spin is flipped which is energetically very inefficient, very high domain boundary energy will be present between the parallel and anti-parallel spins. (c) A ferromagnet in a low energy excited state, all the spins make a precession movement which is brings the ferromagnet out of the ground state. The neighbouring spins are coupled by the Heisenberg interaction and will follow the precession movement with an added phase [3].

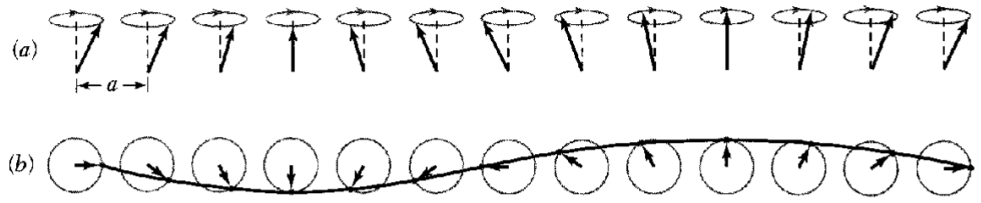

FIGURE 1.2: (a) A depiction of a spin wave, where each neighbouring spin has a slight phase change. (b) The topview of these spins, where a line is drawn through the ends of each spin vector, this results in a periodic wave, which is called a magnon [3].

one spin is anti-parallel. This is however energetically inefficient and it requires high energy to make this excitation, see figure 1.1(b). There is a third option which requires low energy to excite the ferromagnet, see figure 1.1(c). In this state all the spins will make a precessing movement, where the neighbour of each spin will follow the precession with a slight phase difference. The precession results in the spin vector being slightly smaller in the direction it first was, thus collectively one spin is still anti-parallel. Now if a line is drawn through the end of all these spin vectors, as in figure 1.2(b), it will end up as a periodic wave. This wave is called a magnon, a wave of spin-excitation.

1.3 Anomalous Hall Effect

The Hall effect was discovered by E.H. Hall in 1879 [4]. This Hall effect is where a magnetic field perpendicular to the propagation direction of a current causes an orthogonal electromotive force, which is called the Lorentz force. Two years later E.H. Hall found that the electromotive force was ten times larger for ferromagnetic iron [5] than in non-magnetic conductors. This effect is called the Anomalous Hall Effect and will the main topic of this thesis.

1.4 Motivation and Outline

Using magnons instead of electrons for electronic devices can come with many benefits. For example, these magnons can have very high frequencies, ranging from a few dozen GHz to a few THz. If these magnons could be implemented into the integrated circuits it would be possible to make computing devices with a clockrate much higher than is used in current day electronic devices, which have a clockrate on the order of GHz, since the clockrate is directly related to the frequency of the magnon [6]. Another benefit of using magnons is that it allows wavebased computing, where vector operations are used instead of scalar variable operations, this results in less logic operations necessary to compute the same thing. Furthermore magnons allow operations with wavelengths below $10\,nm$ and miniaturization of the devices goes along with an increase of computing speed. Even more applications besides these are being worked on [6].

To make integrated circuits based on magnons it is of course important to know as much as possible about the behaviour of the magnon, otherwise unwanted potential differences or leakage current could appear in a fabricated device, e.g. a travelling magnon gains some transverse velocity due to some unknown Hall effect. Therefore this research will be on the Anomalous Hall Effect (AHE) for magnons. By getting a better understanding of this mechanism the total understanding of the magnon grows, which eases the application of magnons in current day devices. This thesis consists of the following chapters, each provided with a short description:

- *Chapter 2: Theory* - This chapter will start with explaining the magnon itself in more detail and the different ways these magnons can be excited. It will give some information about Yttrium Iron Garnet (YIG), which is the material through which the magnon transport will find place. The Spin Hall Effect will be explained, which is a method of exciting the magnons, and the Inverse Spin Hall Effect and Spin pumping are explained which are a method of detecting the magnons. The Anomalous Hall Effect will be explained in detail, where each contribution to the AHE for electrons will be discussed. [Berry´s phase and curvature will be explained shortly, together with the Dzyaloshinskii Moriya Interaction. These two can be used to predict the AHE for magnons]. Then a few phenomenological hypothesis for the AHE for magnons are drawn by making a comparison to the AHE for electrons. Furthermore a transport mechanisms of the magnon, namely the Spin Seebeck Effect, will be explained. Finally the Stoner Wohlfarth Model will be discussed, because the measurements rely on rotating the magnetization of the YIG from in plane to out of plane by rotating a magnetic field. The magnetization will behave different due to the anisotropy of the film among other things.

- *Chapter 3: Experimental Methods* - The fabrication of the device, that is, the cleaning, the Electron Beam Lithography steps, the development and the deposition of Platinum wires and Titanium/Gold contacts will be explained. The explanations will be more general, to sketch a good overview of how the device is created. All the exact steps taken are listed in Appendix A. Furthermore, the deposition techniques sputtering and electron beam evaporation will be explained, how they work and why one or the other is used. Finally the measurement setup and the way how a signal is sent through and the technique how to measure this signal is explained.

- *Chapter 4: Results and Discussion* - First a comparison will be drawn between measurements from 100 nm thick YIG with previously reported measurements done on 200 nm thick YIG. The Spin Magnetoresistance, local Spin Seebeck voltage of the second harmonic, magnetization of the YIG and the non-local in plane measurements will all be compared to better understand how the thinner YIG affects these mechanisms and ultimately how this could have an influence on the AHE for magnons. Then the out of plane measurements follow, where the Stoner Wohlfarth model will be applied and discussed and finally the resulting measurements are compared with the hypotheses earlier made about the AHE for magnons in chapter 2.

- *Chapter 5: Conclusion* - All the measurements taken will be concluded. Any reasons for the results found will be reported such as the reason why the AHE for magnons was not observed.

Chapter 2

Theory

The theory below will first familiarize the reader with the concept of magnons, how they look like and how they are excited. Then the material Yttrium Iron Garnet (YIG), which will be the material through which the magnons are transported, will be explained along with the properties of the YIG which make it such a good material to use for the magnon transport. Then a section about the (Inverse) Spin Hall Effect follows which explains how a spin-polarized current is generated at the interface between an injector and the YIG and how a current is generated from a spin imbalance in a wire. Also the sign of this (I)SHE, which is a topic of many discussions, will be explained. Thereafter spin pumping is explained, the process of how a magnon gets absorbed and creates a signal in the detector. Then the Anomalous Hall Effect (AHE) for electrons will be explained in detail including the three contributions that exist for the AHE for electrons. After this a section follows about the Anomalous Hall Effect for magnons, where a few phenomenological hyptheses are made in comparison with the AHE for electrons. Then the Spin Seebeck Effect is explained, which is a transport mechanism of the magnons. Finally the Stoner Wholfarth model will be explained, since the magnetization of the YIG will not always be parallel to a rotating magnetic field due to anisotropy among other things.

2.1 Magnons

The magnon dates back to 1930, when F. Bloch studied ferromagnetic behaviour at low temperatures and in specific under what conditions ferromagnetism would be possible at all [7]. He studied a ferromagnet at absolute temperature which, according to the Heisenberg theory, should have all the magnetic moments pointing in the same direction to achieve the lowest energy state, the ground state. If the temperature would then

increase the magnetic moments will start to deviate and the net magnetization will be reduced. If the state of magnetization at zero temperature would be considered as a vacuum state, the deviations at higher temperature can be considered as some gas of quasi-particles. It is these particles that are called magnons and in this case it would be a thermally excited magnon.

The above description gives a phenomenological explanation of the magnon, however nowadays the magnon can be defined much more exact. As follows from the introduction, section 1.2, the magnon is a quantized spin-wave. To explain in depth how this spin-wave looks like we starts with a ferromagnet in its ground state. The magnetization of this ferromagnet can be described by the Landau-Lifshitz-Gilbert equation

$$\frac{d\boldsymbol{m}}{dt} = -\gamma \boldsymbol{m} \times H_{\text{eff}} + \alpha \boldsymbol{m} \times \frac{d\boldsymbol{m}}{dt} \tag{2.1}$$

where $\boldsymbol{m}$ is the magnetization vector, γ is the gyromagnetic ratio, H_{eff} is the effective magnetic field including the external, demagnetization and crystal anisotropy contributions and α is the damping factor, a dimensionless constant [8]. Now the ground state of a ferromagnetic material has all the spins aligned in the same direction from a classical view, as seen in figure 1.1(a). Now the nearest neighbour spin is coupled by the Heisenberg interaction [3],

$$U = -2J \sum_{p=1}^{N} \boldsymbol{S}_p \cdot \boldsymbol{S}_{p+1} \tag{2.2}$$

where J is the exchange integral and $\boldsymbol{S}_p$ and $\boldsymbol{S}_{p+1}$ is spin p and its nearest neighbour. An excitation of this ferromagnet can be seen as one spin which has an opposite direction as in figure 1.1(b). However this is an excitation of high energy as can be seen from equation 2.2. An excitation of lower energy can also be formed by sharing the antiparallel spin over all the spins. These spins will make a precessing motion, as can be seen from figure 1.1(c) and the first term on the right-hand side of equation 2.1. Following the Heisenberg interaction, equation 2.2 the neighbouring spin of a precessing spin will follow the precession motion with an added phase. Now a line can be drawn through the end of the spin vector of each spin and its nearest neighbours and a wave can be seen. This wave, an excitation of spin precession motion, is called the magnon. These magnons are oscillations in the relative orientation of spins on a lattice. Phonons, which are oscillations in the relative position of the atoms on a lattice are analogous to the magnons [3]. Because of this analogy magnons can react with phonons, which is the only interaction for magnons in the ferrimagnetic insulator YIG, which is the material used for magnon transport. At distances shorter than the magnon spin diffusion length the diffusive transport caused by scattering with phonons is dominating [1]. The magnon

spin diffusion length can be described as follows

$$\lambda = \sqrt{D\tau} \tag{2.3}$$

where λ is the magnon spin diffusion length in YIG, D is the magnon diffusion constant and τ the magnon relaxation time, which are both material properties. The magnon relaxation is dominating for large distances [1].

2.1.1 Magnon Excitation

There are two types of magnons that can be excited. The first is by the exchange interaction and the second by dipole-dipole interaction. The difference between these two magnons lies in their frequency, $> 1\,THz$ and $< 100\,GHz$, respectively [6]. The magnons that are discussed in this thesis are the exchange interaction magnons. These exchange magnons are excited by two different ways. Both are excited by sending an AC current through a platinum strip on top of YIG. The first kind of magnons are excited by a polarized spin current at the Pt|YIG interface. This spin polarized current is generated on accord of the Spin Hall Effect (SHE), which will be explained in section 2.2.1. Then by virtue of the exchange interaction, which will also be explained later on, the conduction electrons transfer their angular momentum to the YIG, exciting a magnon and flipping the spin polarization direction [1]. The second method is by ways of Joule heating. The current going through the Pt strip will heat the platinum, thus introducing thermal energy to the YIG. This heating goes as follows:

$$H \propto I^2 \cdot\ R \cdot\ t \tag{2.4}$$

where H is the heating, I the current going through the wire, R the resistance of the wire and t the time. The thermal energy will add to the ground state, thus exciting the YIG. This excitation will generate magnon spin currents, which is similar as described in section 2.1. These two magnons can be differentiated from each other by using lock-in measurement techniques and will be addressed as first harmonic and second harmonic, respectively.

2.2 Yttrium Iron Garnet

Yttrium Iron Garnet ($Y_3Fe_5O_{12}$)(YIG), see figure 2.1 has been a very important material in research on the physics of magnets [10]. YIG is a ferrimagnetic electrical insulator, with a Curie temperature of $T_C = 560K$, which makes experimenting at room temperature

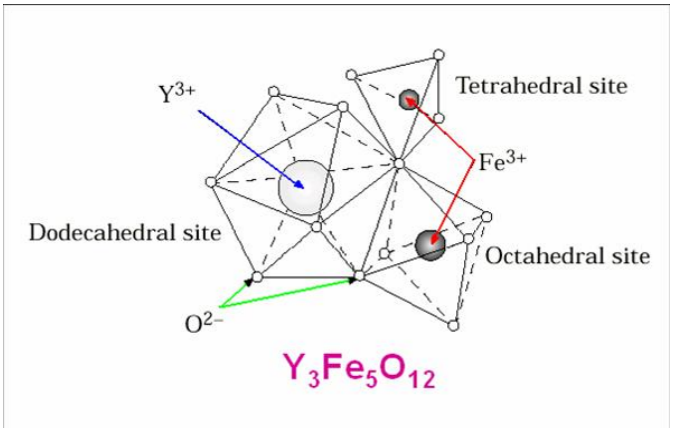

FIGURE 2.1: Crystal lattice structure of YIG where the Yttrium ion is shown with respect to two Fe^{3+} ions, one on a tetrahedral site and the other on an octahedral site [9].

possible. YIG also has a very low Gilbert damping, which is a material property that governs how many rotations a magnetization precession makes before going back to the ground state. Furthermore YIG can be grown with very little defects, which could scatter the magnons, because of the small lattice mismatching of the substrate it is grown on, Gadolinium Gallium Garnet ($Gd_3Ga_5O_{12}$, GGG). The crystal growth is so well perfected that its acoustical damping is lower than that of quartz [10].

The magnetic moment of the YIG is due to the Fe^{3+} ions in the crystal. Three Fe^{3+} ions are located on tetrahedral sites and two Fe^{3+} ions are located on octahedral sites, such as the ones shown in figure 2.1. Through the oxygen ions of the YIG each pair of Fe^{3+} ions on the same site is anti-ferromagnetically coupled. This leaves one Fe^{3+} ion on the tetrahedral site which is not coupled, thus resulting in a net magnetic moment [11].

2.2.1 (Inverse) Spin Hall Effect

The magnon excited by exchange interaction, section 2.1.1, will be excited due to a spin-polarization current at the wire YIG interface. This spin-polarized current is generated by the Spin Hall Effect (SHE). Then by exchange interaction the spin will transfer its angular momentum to the YIG where it excites a magnon and flips the spin-polarization of the electron. The magnon detection will be due to a spin-polarized current, excited by magnons transferring their angular momentum, thus flipping the spin of an electron, in the detector strip. This spin-polarized current will generate a voltage due to the Inverse Spin Hall Effect (ISHE). The transfer of the angular momentum will be explained in section 2.3

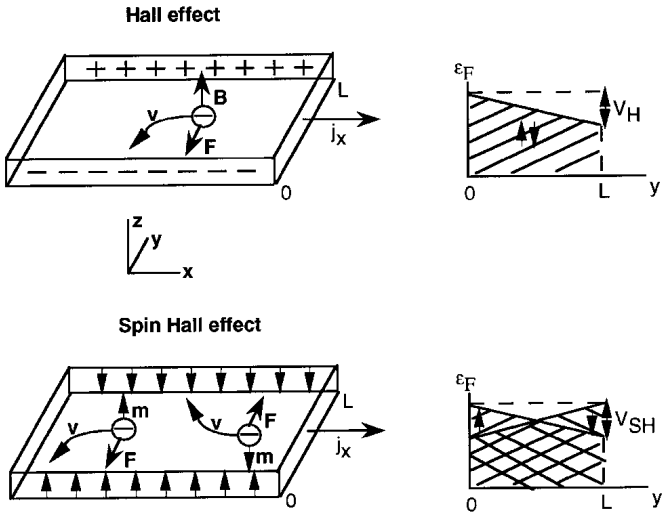

FIGURE 2.2: (a) Depiction of the Hall effect, a magnetic field is placed perpendicular to the current direction, this causes the electrons to experience a Lorentz force orthogonal to the current direction and the magnetic field direction, which creates a potential difference transverse to the current direction. (b) Depiction of the Spin Hall Effect, the same magnetic field is applied to a material with spinorbit coupling, this causes the spins to scatter asymmetrically in the transverse direction and results in a spin potential in the transverse direction [12]

Now consider a material where there is no net magnetization, a material with strong spin-orbit coupling, such as the paramagnetic metal Platinum (Pt). Due to the skew-scattering contribution of the AHE for electrons, as will be explained in section **??**, the electrons of opposite spin and magnetic moment will deflect to opposite directions [12] as can be seen in figure 2.2. This was proposed and proven by Hirsch [12].

This asymmetric scattering can be understood to originate from spin-orbit interaction. First consider an unpolarized beam of electrons incident on a spinless scatterer, the potential of this beam being

$$V = V_c(r) + V_s(r)\sigma \cdot L \tag{2.5}$$

where σ and L are the electron spin and angular momentum respectively, V_s is the usual spin-orbit scattering potential, r is the particle coordinate and V_c is the well depth for forward scattering [13]. The scattered beam will have a spin polarization vector

$$P_f = \frac{fg^* + f^*g}{\mid f \mid^2 + \mid g \mid^2}\hat{n} \tag{2.6}$$

with $\hat{n}$ the unit vector perpendicular to the scattering plane, in direction $k_i \times k_f$, where k_i and k_f are the initial and final scattered wave vectors respectively. f and g are the spin-independent and spin-dependent parts of the scattering amplitude respectively. Particles that scatter to the left and right of the scatterer will have an opposite sign due to

Material	θ_{SH}
Ta	-0.12
Pt	0.067 ± 0.006
Au(Pt)	0.12 ± 0.04
Au	0.016 ± 0.003
Mo	-0.0023 ± 0.0005

TABLE 2.1: θ_{SH} for several materials, where the sign of the spin Hall angles is chosen by convention [14]&[15]. The direction of the SHE can then be described according to the right-hand-rule as proposed in section 2.2.1.2

$\hat{n}$ being opposite. This results in an asymmetry of the spin polarization after scattering. This asymmetry is a direct consequence of the Spin Hall Effect (SHE). Furthermore a characteristic ratio called the Spin Hall angle can be defined where

$$\theta_{SH} \propto \frac{J_s}{J_c} \tag{2.7}$$

where J_s is the transverse spin current density and J_c the applied charge current density. This relation is a measure of how large the spin polarized current will be, the larger θ_{SH}, the bigger the spin polarized current. For materials such as platinum, tantalum and platinum-doped gold and other metals, the θ_{SH} is found in table 2.1. The Spin Hall angles for tantalum and platinum are quite large in comparison with other materials.

2.2.1.1 Inverse Spin Hall Effect

The Inverse Spin Hall Effect (ISHE) is the reciprocal of the SHE, where it starts off with a spin current in a metal with no net magnetization, for example the paramagnetic material platinum. This spin-polarized asymmetry is caused by the spin pumping of the magnons into this metal, where all the spin is dependent on the magnetization direction of the applied magnetic field, see section 2.3. It is expected that the spin-orbit interaction responsible for the SHE can also be responsible for the reverse process to happen [16].

The spin-orbit interaction causes an electric field transverse to the spin current ($\boldsymbol{J}_s$) and spin-polarization factor of the spin current (σ), see figure 2.3, so that

$$\boldsymbol{E}_{\mathrm{ISHE}} \propto \boldsymbol{J}_s \times \boldsymbol{\sigma} \tag{2.8}$$

The dc voltage $\boldsymbol{V}_{ISHE}$ is due to the ISHE induced by spin pumping, so that

$$\boldsymbol{V}_{\mathrm{ISHE}} \propto \boldsymbol{J}_s \cos\theta_m \tag{2.9}$$

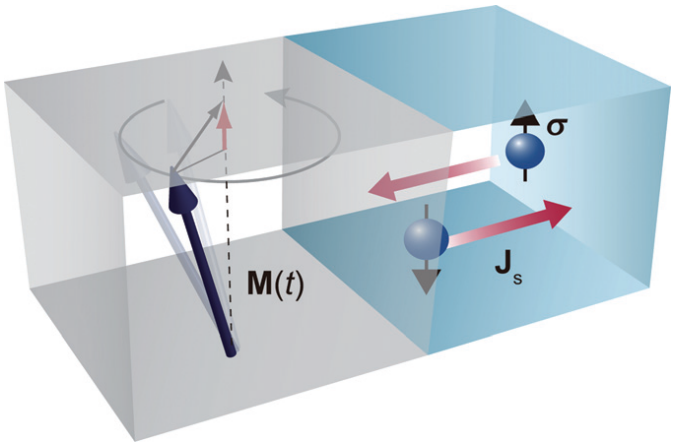

FIGURE 2.3: Schematic illustration of the spin pumping. $\boldsymbol{M}(t)$ is the magnetization of the ferromagnet. $\boldsymbol{J}_s$ and $\boldsymbol{\sigma}$ are the direction and polarization vector of the spin current respectively [16]

where θ_m is the angle of the magnetization with the sample plane where the magnetization is parallel to the spin-polarization direction at 0 degrees [16]. Only the component transverse to this direction will be measured, thus a $\cos(\theta_m)$ magnitude is expected.

2.2.1.2 Sign of the (Inverse) Spin Hall Effect

The sign of the (I)SHE has been a subject of controversy, since defining a sign is subject to the conventions used for the Spin Hall angle, which were not always defined the same way. The sign of an electron $(-e)$ is negative by convention for example. Schreier et al. [17] suggests that the (I)SHE for materials with positive spin Hall angle, such as Pt, can be described using a right-hand-rule. This right-hand-rule is applied as follows, see figure 2.4. With the forefinger point into the direction the electron is moving, which is the direction of the spin pumping in case of the measurements done in this thesis, which will be explained in chapter 4. With the thumb point in the direction of the spin-polarization of the electron. Now the electron will deflect into the direction given by the middle finger.

2.3 Spin Pumping

The magnetization of a ferromagnetic material makes a precessing movement around the direction of an applied magnetic field, which can be seen from the first term on the right-hand side of equation 2.1. When a ferromagnetic material is in contact with a normal metal this precessing movement is damped and transferred to the normal metal, this process is called spin pumping [8].

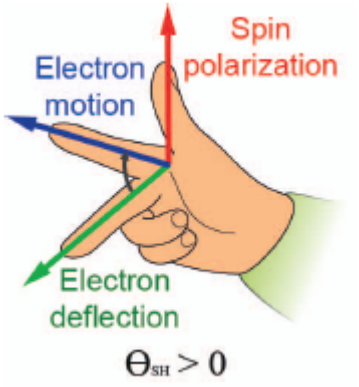

FIGURE 2.4: Right hand rule to determine the direction of the SHE for positive spin Hall angle. The three vectors are orthogonal to each other and if the direction of two vectors are known, the direction of the third can be determined by using the above mnemonic [18].

The precession of the magnetization is caused by the torque of the applied magnetic field, $\boldsymbol{H}_{\text{eff}}$, on the localized magnetic momentum, $\boldsymbol{m}$, where

$$\tau \propto m \times H_{eff} \tag{2.10}$$

where τ is the torque. This torque can be seen as a physical equivalent of a volume injection of a spin current. Normally the precession of a spin dissipites, where the spin will return to its ground state after making a certain number of turns, this dissipation is called the Gilbert damping and is a material property. If the spin current can exert some torque on the magnetization results in an increase or decrease of the precession angle, the inverse would be that the changing angle of precession can excite a spin current by using the torque. This is what happens when a precession in a ferromagnetic material can leak into a normal metal. This damping of the torque by exciting a spin current is then called the enhanced Gilbert damping [8].

The precessing magnetization is a source of non-equilibrium spin accumulation where the spin-polarization directions are all dependent on the magnetic moment [8]. The magnetic moment of of an atom can be given as follows

$$\boldsymbol{\mu} = \frac{-e}{2m} \mid \boldsymbol{l} \mid \tag{2.11}$$

where $-e$ is the total charge of the atom and l is the angular momentum of the atom. This magnetic moment will accumulate spins which have the following magnetic moment

$$\boldsymbol{\mu}_s = \frac{-e}{2m} g_s \boldsymbol{s} \tag{2.12}$$

where g_s is the g-value of the spin, which is approximately 2 and s is the angular momentum of the spin. Aligning the magnetic momenta of the spins will be at the the cost of the magnetic momentum of the atom and therefore at the cost of the angular momentum of the atom. From equation 2.12 it follows that the magnetic moment and spin-polarization direction are antiparallel to each other. These spins then dissipates in the normal metal by spin-flip processes as a spin current.

2.4 Anomalous Hall Effect

In 1879 E. H. Hall reported about the effect of out of plane magnetic fields on electric currents where he discovered that there is an electromotive force working transverse to the current direction [4]. This later became known as the Hall Effect. Two years later in 1881 E. H. Hall reported that an electromotive force, larger than observed for the Hall effect, was observed for a ferromagnetic material [5]. This second discovery is now know as the Anomalous Hall Effect (AHE).

The Hall effect for electrons is normally driven by a Lorentz force, but for charge-free particles, like photons, phonons and magnons, there is no Lorentz force to drive any Hall effect. However, in a ferromagnetic material, the Hall effect is proportional to the magnetization and can be driven by the relativistic spin orbit interaction [19]. This effect is called the Anomalous Hall Effect (AHE). This AHE has been theoretically proven and experimentally observed for photons and phonons, [20] & [21]. To understand the AHE for electrons it is necessary to understand what is a Berry phase and Berry curvature. Then the AHE for electrons and mainly its mechanisms can be discussed. Thereafter a few phenomenological hypotheses are drawn for the AHE for magnons where a similarity will be drawn to the AHE for electrons.

2.4.1 Berry´s Phase & Berry Curvature

To explain how the Hamiltonian of a system changes under an adiabatic process an example taken from Griffiths and Harris [22] will be started with. Begin with a pendulum and start swinging it in one direction while on the north pole of the earth, see figure 2.5. Now if this pendulum is transported adiabatically towards Amsterdam in a straight longitudinal line, then transported toward the USA across a latitudinal line and then returned to the north pole again along a longitudinal line. Arriving at the north pole it can be observed that the pendulum is not swinging in the direction it started with but it has gained a phase. This same concept can be applied to the Hamiltonian of a system and the added phase is called Berry´s phase.

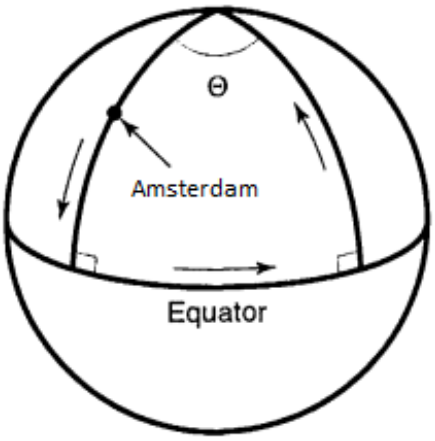

FIGURE 2.5: Adiabatic path of a pendulum across earth. The pendulum gains an angle Θ [22]

Previously Griffiths and Harris [22] showed that a particle in the nth eigenstate of $H(0)$, under adiabatic conditions, stays in the nth eigenstate of $H(t)$ picking up only a time-dependent phase factor. Specifically, the wave-function of such a particle can be given as

$$\Psi_n(t) = e^{\mathrm{i}[\theta_n(t)+\gamma_n(t)]} n(t) \tag{2.13}$$

where $\theta_n(t)$, the dynamic phase, is described as

$$\theta_n(t) \equiv -\frac{1}{\hbar}\int_0^t E_n(t')dt' \tag{2.14}$$

and $\gamma_n(t)$, the geometrical phase, is described as

$$\gamma_n(t) \equiv \mathrm{i}\int_0^t \langle n(t') \mid \frac{\partial}{\partial t'} n(t')\rangle dt' \tag{2.15}$$

Now the wave-vector of this particle is time-dependent, since there is some parameter, $\boldsymbol{R}(t)$, in the Hamiltonian which is changing with time. Now the following can be written

$$\frac{\partial n(\boldsymbol{R})}{\partial t} = \frac{\partial n(\boldsymbol{R})}{\partial \boldsymbol{R}}\frac{d\boldsymbol{R}}{dt} \tag{2.16}$$

and with this equation 2.15 can be rewritten as

$$\begin{aligned}\gamma_n(t) &= \mathrm{i}\int_0^t \langle n(\boldsymbol{R}) \mid \frac{\partial n(\boldsymbol{R})}{\partial \boldsymbol{R}}\rangle \frac{d\boldsymbol{R}}{dt'}dt' \\ &= \mathrm{i}\int_{\boldsymbol{R}_i}^{\boldsymbol{R}_f} \langle n(\boldsymbol{R}) \mid \frac{\partial n(\boldsymbol{R})}{\partial \boldsymbol{R}}\rangle \cdot d\boldsymbol{R} \\ \gamma_n(C) &= \mathrm{i}\oint \langle n(\boldsymbol{R}) \mid \nabla_{\boldsymbol{R}} n(\boldsymbol{R})\rangle \cdot d\boldsymbol{R}\end{aligned} \tag{2.17}$$

where $\boldsymbol{R}_i$ & $\boldsymbol{R}_f$ are the initial and final values of $\boldsymbol{R}(t)$. The last equation describes the net geometric phase change after time of a Hamiltonian returning to its original form. This geometric phase change is known as Berry´s phase [23], which is a line integral around a closed loop (C) in parameter-space. Evaluating $\mid \nabla_{\boldsymbol{R}} n(\boldsymbol{R})\rangle$ requires a locally single valued basis for $\mid n(\boldsymbol{R})\rangle$ which can be difficult to work with. To avoid this Berry [23] transforms equation 2.17 using Stokes´ Theorem to a surface integral whose boundary is C instead of a phase change along C

$$\begin{aligned}\gamma_n(C) &= -\mathrm{Im}\int\int_C d\boldsymbol{S}\cdot\nabla\times\langle n \mid \nabla n\rangle \\ &= -\mathrm{Im}\int\int_C d\boldsymbol{S}\cdot\langle\nabla n \mid \times \mid \nabla n\rangle \\ &= -\mathrm{Im}\int\int_C d\boldsymbol{S}\cdot\sum_{n'\neq n}\langle\nabla n \mid n'\rangle\times\langle n' \mid \nabla n\rangle\end{aligned} \tag{2.18}$$

where $d\boldsymbol{S}$ denotes an area element in R space. The off-diagonal elements are given as

$$\langle n' \mid \nabla n\rangle = \langle n' \mid \nabla\hat{H} \mid n\rangle/(E_n - E_m), \qquad n' \neq n \tag{2.19}$$

Taking this into account γ_n can be defined as

$$\gamma_n(C) = -\int\int_C d\boldsymbol{S}\cdot\boldsymbol{V}_n(\boldsymbol{R}) \tag{2.20}$$

where $\boldsymbol{V}_n$ is the term for the Berry curvature and is given as

$$\boldsymbol{V}_n(\boldsymbol{R}) = \mathrm{Im}\sum_{n'\neq n}\frac{\langle n(\boldsymbol{R}) \mid \nabla_{\boldsymbol{R}}\hat{H}(\boldsymbol{R}) \mid n'(\boldsymbol{R})\rangle\times\langle n'(\boldsymbol{R}) \mid \nabla_{\boldsymbol{R}}\hat{H}(\boldsymbol{R}) \mid n(\boldsymbol{R})\rangle}{(E_m(\boldsymbol{R}) - E_n(\boldsymbol{R}))^2} \tag{2.21}$$

This Berry curvature is the curl from the vector, as can be seen from 2.21, of the travelling particle or system. So by knowing the trajectory of the particle or system it is possible to calculate the geometrical phase change.

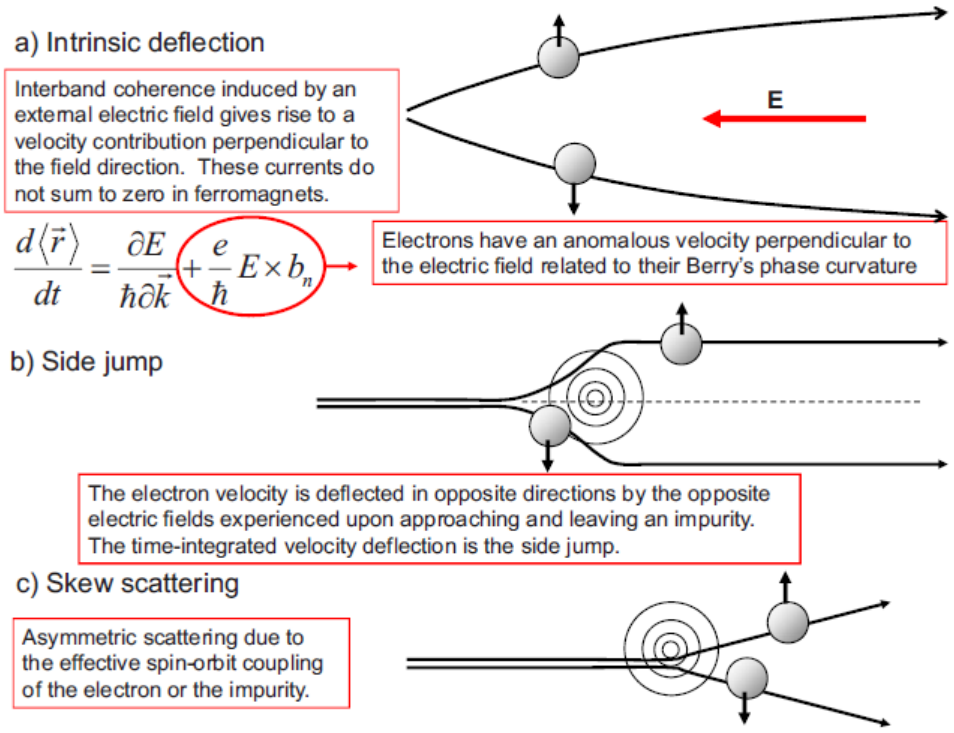

FIGURE 2.6: The three contributions to the Anomalous Hall Effect for electrons [24]

2.4.2 The Anomalous Hall Effect for electrons

The Anomalous Hall Effect (AHE) for electrons has three contributions, the intrinsic deflection, side jumps and skew scattering [24]. The total AHE due to these three contributions can be written as

$$\sigma_{xy}^{AH} = \sigma_{xy}^{AH-int} + \sigma_{xy}^{AH-skew} + \sigma_{xy}^{AH-sj} \tag{2.22}$$

where each σ is the corresponding contribution. The xy component of the contribution suggests that the conductivity in the transverse direction to the current direction is of interest, since this is the direction of any Hall effects. The applied magnetic field in this case would be in the z-direction and the current in the x-direction. The three components can be seen in figure 2.6

2.4.2.1 Intrinsic Contribution to σ_{xy}

The easiest to evaluate of these three contributions is the intrinsic contribution, see figure 2.6(a). The intrinsic contribution is only dependent on the band conductivity of a perfect crystal. It can be directly derived from Kubo´s formula for the Quantum Hall

conductivity [25], which goes as follows

$$\sigma_H = \frac{\mathrm{i}e^2}{A_0\hbar} \sum_{\epsilon_\alpha < E_F} \sum_{\epsilon_\beta > E_F} \frac{(\frac{\partial \hat{H}}{\partial \boldsymbol{k}_1})_{\alpha\beta}(\frac{\partial \hat{H}}{\partial \boldsymbol{k}_2})_{\beta\alpha}) - (\frac{\partial \hat{H}}{\partial \boldsymbol{k}_2})_{\alpha\beta})(\frac{\partial \hat{H}}{\partial \boldsymbol{k}_1})_{\beta\alpha})}{(\epsilon_\alpha - \epsilon_\beta)^2} \tag{2.23}$$

where A_0 is the area of the system, ϵ_α and ϵ_β are eigenvalues of the Hamiltonian H, $\boldsymbol{k}_1$ and $\boldsymbol{k}_2$ are two dependent variables of the Hamiltonian. When the eigenstates $\mid n, \boldsymbol{k}\rangle$ and eigenvalues $\epsilon_n(\boldsymbol{k})$ of a Bloch Hamiltonian are given, then the intrinsic contribution to the AHE can be written as

$$\begin{aligned} \sigma_{ij}^{AH-int} = e^2\hbar \sum_{n \neq n'} \int \frac{d\boldsymbol{k}}{(2\pi^d)} [f(\epsilon_n(\boldsymbol{k})) - f(\epsilon_{n'}(\boldsymbol{k}))] \\ \times \mathrm{Im} \frac{\langle n, \boldsymbol{k} \mid v_i(\boldsymbol{k}) \mid n', \boldsymbol{k}\rangle \langle n', \boldsymbol{k} \mid v_j(\boldsymbol{k}) \mid n, \boldsymbol{k}\rangle}{[\epsilon_n(\boldsymbol{k}) - \epsilon_{n'}(\boldsymbol{k})]^2} \end{aligned} \tag{2.24}$$

where the Hamiltonian is only dependent on $\boldsymbol{k}$ for the periodic part of the Bloch function. The velocity in equation 2.24 is defined by

$$\boldsymbol{v}(\boldsymbol{k}) = \frac{1}{\mathrm{i}\hbar}[\boldsymbol{r}, H(\boldsymbol{k})] = \frac{1}{\hbar}\nabla_{\boldsymbol{k}} H(\boldsymbol{k}) \tag{2.25}$$

The phenomenological description of the intrinsic contribution can be given as follows. The intrinsic contribution is dependent on the periodic potential of the perfect crystal lattice, which are the Bloch states, so the contribution is directly linked to the topological properties of the material. To be more specific the contribution is proportional to the integral of the Berry phases over the Fermi-surface segments [26]. Using equation 2.19 it is possible to rewrite equation 2.24 to

$$\sigma_{ij}^{AH-int} = -\epsilon_{ijl}\frac{e^2}{\hbar} \sum_n \int \frac{d\boldsymbol{k}}{(2\pi)^d} f(\epsilon_n(\boldsymbol{k})) b_n^l(\boldsymbol{k}) \tag{2.26}$$

where ϵ_{ijl} is the antisymmetric tensor and $b_n(\boldsymbol{k})$ is the Berry curvature

$$b_n(\boldsymbol{k}) = \nabla_{\boldsymbol{k}} \times a_n(\boldsymbol{k}) \tag{2.27}$$

where $a_n(\boldsymbol{k})$ is the Berry-phase connection, $a_n(\boldsymbol{k}) = \mathrm{i}\langle n, \boldsymbol{k} \mid \nabla_{\boldsymbol{k}} \mid n, \boldsymbol{k}\rangle$, which correspond to the states $\{\mid n, \boldsymbol{k}\rangle\}$. This Berry connection is a geometric vector potential, the vector being the travelled path.

The intrinsic contribution to the AHE only depends on topological factors, which makes this contribution easy to evaluate accurately for electrons transported through a ferromagnetic material. For many ferromagnetic materials with strong spin-orbit coupling, this intrinsic contribution dominates the AHE [24].

2.4.2.2 Skew-scattering contribution to σ_{xy}

The skew-scattering contribution to the AHE is simply proportional to the Bloch state transport lifetime, see figure 2.6(c). Therefore in a more perfect crystal lattice the skew-scattering contribution is dominating the AHE. This contribution is the only contribution which can be completely described according to the Boltzmann transport theory

$$\frac{\partial f}{\partial t} + \boldsymbol{v} \cdot \mathrm{grad}_{\boldsymbol{r}} f + \alpha \cdot \mathrm{grad}_{\boldsymbol{v}} f = \frac{\partial f}{\partial t}_{\mathrm{coll}} \tag{2.28}$$

where f is the classical distribution function in the six-dimensional space of Cartesian coordinates $\boldsymbol{r}$ and velocity $\boldsymbol{v}$, α is the acceleration $\frac{d\boldsymbol{v}}{dt}$ and $\frac{\partial f}{\partial t}_{\mathrm{coll}}$ is the collision term [3]. This equation describes the probability of a number of particles in a volume element, with a certain velocity. If this volume element is followed along a flow-line the distribution will be conserved. Furthermore in this volume element particles can accelerate away from each other or can collide with each other or travel unaffected [3].

The semi-classical Boltzmann transport theory states that the transition probability $W_{n\to m}$ is identical to the transition probability $W_{m\to n}$. However, in a microscopic sense this balance does not always hold [24]. For a material with spin-orbit coupling both the Hamiltonian of the perfect crystal lattice and the disorder Hamiltonian can have different transition probabilities when travelling in opposite directions. When these transition rates are evaluated the asymmetric chiral contribution arises as a third order process in the disorder scattering [24], because at that point the detailed balance of the semi-classical Boltzmann theory will fail, which will be present in the perturbation introducing the transition. In simplified models this asymmetric chiral contribution to the transition probability can be written as

$$W^A_{\boldsymbol{k}\boldsymbol{k}'} = -\tau_A^{-1} \boldsymbol{k} \times \boldsymbol{k}' \cdot \boldsymbol{M}_s \tag{2.29}$$

where $W^A_{\boldsymbol{k}\boldsymbol{k}'}$ is the scattering probability from the incident momentum, $\boldsymbol{k}$, to $\boldsymbol{k}'$, τ is the transport lifetime and $\boldsymbol{M}_s$ is the magnetization Inserting this contribution in the Boltzmann equation will lead to Hall resistivity being proportional to the longitudinal resistivity

$$\rho_H^{skew} = \sigma_H^{skew} \rho^2 \propto \rho \tag{2.30}$$

where ρ_H^{skew} is the resistivity and σ_H^{skew} the conductivity due to the skew-scattering contribution and ρ is the longitudinal resistivity.

The ability to calculate the skew-scattering contribution is limited however, since any defects in the crystal lattice have no way of being defined periodically. These defects

are mostly random and thus is it only possible to give proportions instead of a distinct magnitude.

2.4.2.3 Side-jump contribution to σ_{xy}

The side-jump contribution is very similar to the intrinsic contribution, see figure 2.6(b) and can be described as follows: When a Gaussian wave packet encounters a spherical defect with spin-orbit interaction it will scatter, where the wave-vector $\boldsymbol{k}$ of the wave packet will experience a displacement transversely to $\boldsymbol{k}$, this displacement is then called a side-jump. This contribution lies outside the bounds of the Boltzmann transport theory and no extrinsic parameters apply to this scattering. Therefore the side-jump contribution is of same order as the intrinsic contribution.

This side-jump contribution however has been very difficult to define and practically impossible to predict [24]. Therefore it is an accepted practice to first evaluate the intrinsic contribution of the AHE according to the intrinsic contribution as described in section 2.4.2.1. If the contribution is independent on σ_{xx} and in agreement with the intrinsic contribution, then there is no side-jump contribution. Any deviations however are identified with the side-jump contribution.

2.4.2.4 Dependence of the contribution on the material conductivity

These three contributions have a different regime of conductivity where they dominate. The first of these regimes is the *High conductivity regime*. In this regime the conductivity $\sigma_{xx} > 0.5 \times 10^6\,(\Omega\,cm)^{-1}$ and the skew-scattering component of the AHE is dominating, in this regime our Pt injector and detector strips are located, since $\sigma_{Pt_{xx}} = 9.52 \times 10^6\,(\Omega\,cm)^{-1}$, therefore the component of the AHE for electrons contributing to the (I)SHE will be due to the skew-scattering of the electrons [12]. The second regime is the *Good metal regime*. In this regime the magnitude of σ_{xy} is independent on σ_{xx}, which lies in the range $\sigma_{xx} \sim 10^4 - 10^6\,(\Omega\,cm)^{-1}$ [27]. This relation suggests that in this regime the scattering-independent mechanisms dominate, so the intrinsic and side jump contributions. None of the materials that are used however are within this regime. The last regime is the *Bad-metal-hopping regime*. In this regime, where $\sigma_{xx} < 10^4\,(\Omega\,cm)^{-1}$, σ_{xy} scales faster than linear with σ_{xx} as is reported by Nagaosa et al. [24]. Also in this regime ρ_{xx} is dependent on the temperature. From these observations it is not clear if there is a component of the AHE which dominates, also there is no theory which predicts the linear scaling in this regime [24]. Also no materials discussed will be in this regime as the YIG is electrical insulation and the magnon transport through the YIG may behave very different to the electrons in this regime.

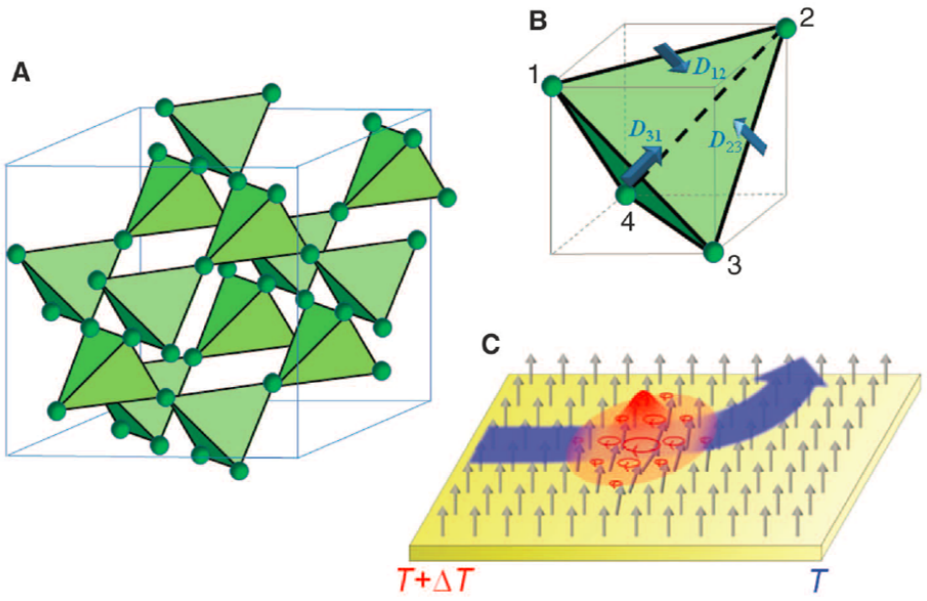

FIGURE 2.7: From [19]. (A) A pyrochlore structure, where (B) the DMI vectors are shown for one of the tetrahedral crystals. (C) The resulting magnon Hall effect observed for magnons travelling through a temperature gradient.

2.4.3 Possible mechanisms for the Anomalous Hall Effect for magnons

While the AHE for electrons has been extensively researched [24], the effect for magnons is a recent subject of interest [19]. The Berry curvature in momentum space, section 2.4.1, for various particles such as electrons, photons, and magnons, can cause Hall effects such as the Spin Hall effect and the thermal Hall effect. Because the Berry curvature originates from the wave nature of these particles, a non-zero Berry curvature of these particles would then manifest as Hall effects [28].

For magnons transport it can be shown that the Dzyaloshinskii-Moriya spin-orbit interaction (DMI) for pyrochlore structures is non-zero and therefore the Berry curvature of the magnon would also be zero, thus the AHE for magnons can be proven and observed for thermal gradients in pyrochlore structures, as can be seen in figure 2.7 and has been shown by Onose et al. [19]. For YIG however it is much more difficult to prove the same, since the crystal structure of the YIG is very complicated, as seen in section 2.2. It is very difficult to quantize the DMI for YIG, because the crystal structure does not show any clear inversion symmetry center or lack thereof.

Therefore from comparison with the AHE for electrons the following two hypotheses can be made for the AHE for magnons:

1. The AHE for electrons shows that charges with opposite spin-polarization direction deflect towards opposite directions, as can be seen from figure 2.6. Therefore if the

magnons have opposite magnetic momentum these magnons should also deflect towards opposite directions.

2. The AHE for electrons has three vectors, the propagation direction of the elctron, the spin-polarization direction and the direction of the deflection. These three vectors are orthogonal to each other. Now if three similar vectors would be defined for magnons, so the propagation direction of the magnon spin current, the magnetic momentum of the magnon and the deflection direction of the magnons, then these three vectors should also be orthogonal to each other.

This last hypothesis can be compared with figure 2.7. In this figure the deflection direction of the magnon is orthogonal to the propoagation direction of the magnon spin current and the magnetic moment of the magnon, so thus far the hypothesis is correct.

2.5 Spin Seebeck Effect

When two rods of the same length but of different material are placed parallel to each other and one end of the rods gets heated, a heat gradient will form along the length of the rod, as can be seen in figure 2.8(a). Now because the rods are of different material the heat in one rod will move more easily than the other. When the other ends of the two rods get connected electrically it is possible to measure a voltage difference due to the difference in heat conductivity of the materials. The phenomenon of the voltage being generated is known as the Seebeck effect [29]. The setup described is called a thermocouple and rate of heat to electricity conversion is called the Seebeck coefficient. This efficiency is governed by the scattering rate and density of conduction electrons.

However, when taking a metallic magnet there is a difference between the scattering rates and densities of spin up- and spin down electrons. When applying a temperature gradient to this type of material it is possible to measure a spin voltage on the other end of the magnet, as can be seen in figure 2.8(b). This effect is then called the Spin Seebeck Effect (SSE) [30]. Furthermore this SSE allows to pass a pure spin current over long distances. A temperature gradient in the YIG can be present due to the Joule heating of the injector strip. This temperature gradient can be detected as a charge signal using the ISHE. The SSE can go much further in the ferromagnetic material than the spin relaxation length of a magnon, which results in the fact that the SSE is measured on the signal of the thermal magnons, due to the way the lock-in amplifiers are used to differentiate between the first and second harmonic magnon.

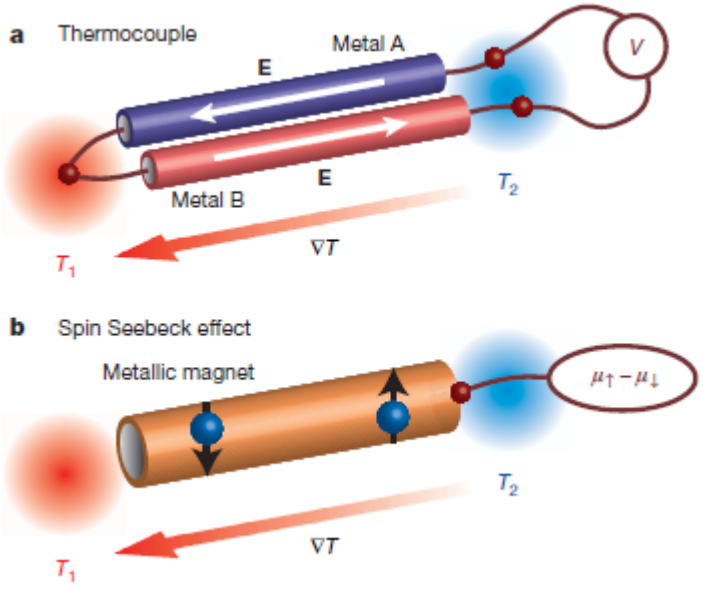

FIGURE 2.8: (a), Image of a thermocouple where metal A and metal B have a different Seebeck coefficient. Applying a temperature gradient to the thermocouple results in a current at the cold end proportional to the difference in Seebeck coefficients. (b), Depiction of the Spin Seebeck effect. The spin-up and spin-down electrons have a different Seebeck coefficient in a metallic magnet and thus a spin potential arises ($\mu_\uparrow - \mu_\downarrow$) at the cold end. This potential is proportional to the difference in Seebeck coefficient of the electrons [30].

2.6 Stoner Wohlfarth Model

Every ferromagnetic material tries to achieve a state minimum energy, as described by equation 2.2. The potential energy is minimum when all the spins are aligned in the same direction and this state is called the ground state of the ferromagnetic material. For ferromagnetic materials with crystal anisotropy the ground state can be more easily achieved in a certain direction than others as described by the following equation

$$\boldsymbol{E}_D = \frac{1}{2}\boldsymbol{I}_0^2(N_1\alpha_1'^2 + N_2\alpha_2'^2 + N_3\alpha_3'^2) \tag{2.31}$$

where α_1', α_2', α_3' are the direction cosines of I_0, the magnetization, N_1, N_2, N_3 are the demagnetization coefficient along different axes of the material, which are different from each other for ferromagnets with crystal anisotropy. E_D describes the energy of an ellipsoid per unit volume associated with the demagnetization fields. When placing a ferromagnetic material in a magnetic field the magnetization will try to align with this magnetic field to achieve a ground state again. This is where E.C. Stoner and E.P. Wohlfarth introduce their theory [31].

When achieving a ground state in a ferromagnet there are several factors which will influence this ground state. The first of these is the boundary movement process, where

magnetic boundaries will form and move to achieve an as low as possible boundary energy. These boundaries are susceptible to stress variations, which means that as a boundary is in equilibrium position and a magnetic field is placed with an angle with respect to the ground state magnetization, this boundary will move reversibly until it reaches some value for which the energy gradient is maximum. At this point the boundary will move spontaneously to a new equilibrium position. This stress variation is the main contributions to the boundary movement process and in ordinary material (material with 10^{10} to 10^{15} atoms) this process would be enough to bring the material in a ground state, where the magnetization points along the easiest directions. However, when considering a heterogeneous alloy, which is a material where more ferromagnetic particles are separated by less ferromagnetic particles, a second process is prrotation process in single domains,es, the ent. In this kind of structure it may not be possible to create boundaries in certain domains. This process can have a greater effect than the boundary movement processes.

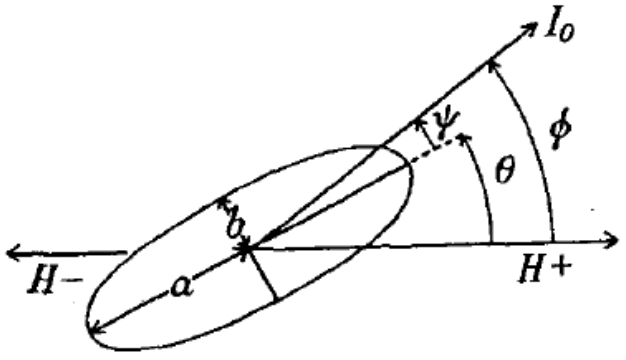

FIGURE 2.9: Definition of the symbols for the SW model [31]

These effect have been generalized by Stoner & Wohlfarth in their model, which goes as follows. Turning an uniformly magnetized ellipsoid about its longer axes will create a prolate spheroid. This prolate spheroid can be seen in figure 2.9. The direction of the equilibrium magnetization of this prolate spheroid lies in a plane constructed by the directions of the applied magnetic field (H) and the polar axis of the ellipsoid. Consequently θ is the angle between the polar axis of the ellipsoid and the positive direction of H. ϕ is the angle of the magnetization direction with the applied field and ψ is the angle of the magnetization with respect to the polar axis of the ellipsoid, so that

$$\phi = \theta + \psi \tag{2.32}$$

For an ellipsoid, the energy per unit volume for spherical coordinates (E_D), as seen in equation 2.31, and the energy associated with an applied magnetic field (E_H) can be

written together as the term for the total relevant energy,

$$\boldsymbol{E}' = \boldsymbol{E}_D + \boldsymbol{E}_H = \frac{1}{4}(N_b + N_a)\boldsymbol{I}_0^2 - \frac{1}{4}(N_b - N_a)\boldsymbol{I}_0^2 cos(2\psi) - \boldsymbol{H}\boldsymbol{I}_0 \cos(\phi) \tag{2.33}$$

where $\boldsymbol{H}$ is the applied magnetic field, $\boldsymbol{I}_0$ is the direction of the magnetization and N_a & N_b are the demagnetization constants along the polar and equatorial axes respectively. Rewriting this obtains the reduced energy,

$$\eta' = \frac{\boldsymbol{E}'}{(N_b - N_a)\boldsymbol{I}_0^2} = \frac{1}{4}\frac{N_b + N_a}{N_b - N_a} - \frac{1}{4}\cos 2\psi \; - \frac{\boldsymbol{H}}{(N_b - N_a)\boldsymbol{I}_0}\cos\phi \tag{2.34}$$

From this the variable part of the energy can be obtained, which is the following

$$\eta = -\frac{1}{4}\cos 2\psi \; - h\cos\phi \tag{2.35}$$

where

$$h = \frac{\boldsymbol{H}}{(N_b - N_a)\boldsymbol{I}_0} \tag{2.36}$$

Here h can be regarded as a variable which gives the rate of magnetization. For a larger applied magnetic field, the material will be more saturated. Equation 2.35 can be rewritten as

$$\eta = -\frac{1}{4}\cos 2(\phi - \theta) \; - h\cos\phi \tag{2.37}$$

Treating h and θ as fixed this equation can be derived to obtain the stationary value of the function given by

$$\frac{\partial \eta}{\partial \phi} = \frac{1}{2}\sin 2(\phi - \theta) \; + h\sin\phi = 0 \tag{2.38}$$

which correspond to the minima, the point of inflexion, and the maxima, respectively, described as follows

$$\frac{\partial^2 \eta}{\partial \phi^2} = cos\, 2(\phi - \theta) \; + h\, cos\, \phi \gtreqless 0 \tag{2.39}$$

The goal of using this model is to get a relation between the angle of the applied magnetic field $\boldsymbol{H}$ with the sample plane, θ, and the angle of the magnetization $\boldsymbol{I}_0$ with the sample plane, ψ. Thus equation 2.38 is rewritten as follows

$$h\, sin\, (\psi - \theta) \; = \; -\frac{1}{2} sin\, \psi \tag{2.40}$$

where $-\theta$ is chosen instead of θ so that it lies in the same direction of the magnetization for clarity, since for higher applied magnetic fields than the saturation field the magnetization closely follows the direction of the applied magnetic field.

A plot of this result with an applied magnetic field twice the saturation magnetization, so that $h = 2$, is shown in figure 2.10. Here the effect of the Stoner Wohlfarth model can be clearly seen. When the angle of the magnetic field increases the magnetization

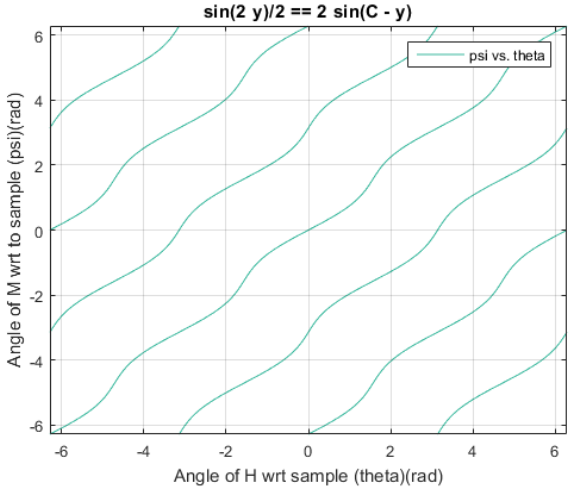

FIGURE 2.10: Plot of psi(y) vs θ(C) for an applied magnetic field twice the saturation field. Even though the material is fully saturated, the magnetization does not completely follow the applied magnetic field.

angle will lag behind until a certain point where an easier direction is reached, then the magnetization angle will catch up with the magnetic field angle and it will even overshoot a little bit because the easy direction is at that point still ahead of the magnetic field angle. This process repeats itself and so the shape in figure 2.10 is created.

Chapter 3

Experimental Methods

The methods used to create and measure the device are explained below. The device is created by standard Electron Beam Lithography procedure and is measured in a 2-lockin measurement setup.

3.1 Device Fabrication

The fabrication of each device starts the same. A layer of $100\,nm$ thick YIG is grown onto the (111) plane of a $500\,\mu m$ layer of $Gd_3Ga_5O_{12}$ by liquid-phase epitaxy (LPE). From this wafer a small piece is cut off and that will be the basis of the device fabrication. All the fabrication steps are explained in detail and step-by-step, in appendix A.

3.1.1 Electron Beam Lithography

The device will be patterned using electron beam lithography (EBL), since the geometry of the device will contain multiple wires of only a few hundred nanometers wide in close proximity to each other. However to successfully do the EBL the sample needs to be cleaned and coated with a layer of photoresist.

- *Cleaning of the Sample* - Every time a new sample is being worked on it will first be cleaned thoroughly. The sample is rinsed with de-ionized water, acetone, isopropanol (IPA) and ethanol, see appendix A. After the cleaning steps have been done the sample can be checked under the optical microscope to see if the dirt is gone under [1000x magnification]. If there is still some left, then the cleaning procedure can be done again.

- *Spin Coating* - To be able to make a pattern on the device it is necessary to place a mask on the device which will protect most of the device except for a few selected areas. This mask is created by first spincoating a layer of photoresist, Poly(methyl methacrylate) or PMMA for short, onto the sample. The PMMA used to for spincoating is PMMA 950K 4%, which gives a $\sim 210\,nm$ thick layer of photoresist after spincoating. The PMMA is spincoated at 4000 rpm for 60 seconds. After spincoating the PMMA an uniform layer should be on the sample. This can be check by placing the sample under the optical microscope, since the YIG is mostly transparent the thickness changes of the PMMA at the edge of the YIG sample will show as a rainbow color. If that is the case, then the middle of the sample has an uniform thick layer of PMMA, onto which the device can be patterned. However, to proceed with the EBL a conducting layer on top of the sample is needed, since neither the YIG or the PMMA can conduct electrons well. To compensate for this a layer of aquaSAVE is spincoated onto the sample. The procedure for spincoating the aquaSAVE is exactly the same apart from it being spincoated at 6000 rpm for 120 seconds. After this is done the sample is once again checked under the optical microscope to see if the spincoated layers are still uniform. If this is the case then the EBL procedure can be started.

- *EBL Procedure* - To make a pattern onto the sample the Raith e-line electron beam system was used. By using EBL on a PMMA mask, which has long chain polymers it is possible to break these polymers into short chain polymers in certain regions, i.e. the regions where the device will be patterned.

- *Development* - After the EBL is done a pattern of short chain polymers will remain. During the development these short chain polymers will be removed while the long chain polymers will stay during the deposition of a material. With the development the sample is put into a developer liquid, MIBK:IPA (3:1) in this case, in which the short chain polymers dissolve. Then after 30 seconds all these short chain polymers should be dissolved and the developing process is stopped by placing the sample in IPA for 30 seconds, otherwise the long chain polymers could also dissolve. After the development is done the material can be deposited onto the sample by ways of sputtering or evaporation, which will be explained in sections 3.1.2 & 3.1.3, respectively. For the samples that were created the Pt wires were sputtered and the Ti/Au contacts were evaporated.

- *Lift-off* - Finally when all of the above has been done the lift-off can be done. The sample is now coated with a layer of either Pt or Ti/Au which needs to be removed from the part which is not patterned. The lift off is done by letting the sample sit in hot acetone for a long time, to fully remove the long chain polymer PMMA

as well. If it is fully developed, a large part of the material deposited won´t be in contact with the sample. This part can be carefully shaken off and results in the EBL pattern remaining on the sample. After all the electrical components, the Pt wires and Ti/Au contacts, are successfully deposited on the sample one last step remains before the sample can be measured. The sample is glued onto a chip-carrier. After the glue has dried the big pads of the sample can be connected with the wiring of the chip-carrier itself. Here one end of a small wire is soldered to one pad of the chip-carrier, then the other end of the wire is soldered and cut to one of the big pads on the sample.

All of the measurement data in this thesis will be done on samples made by the above procedures. Any anomalies are documented in an electronic logbook of which the data can be requested from the author of this thesis.

3.1.2 Sputtering

To create the platinum wires on the device it is necessary that it has a good connection with the YIG to have a high spin mixing conductance and therefore a larger measured signal. This can be achieved by sputtering where a plasma is created which bombards a material source and excites highly charged ions. These highly charged ions then diffuse towards the sample where they bombard the sample from multiple angles, the whole process can be seen in figure 3.1.

The sputtering is done in an argon atmosphere. By placing a big potential difference between the stage where the sample is loaded and the material source the argon will form a plasma [11]. The target material is then set under negative bias so the Argon ions will accelerate towards the target diffusively and therefore hit the target from many angles. This ejects particles from the target which then move towards the substrate. This results in a homogeneous thick layer of the target ions embedded upon the substrate.

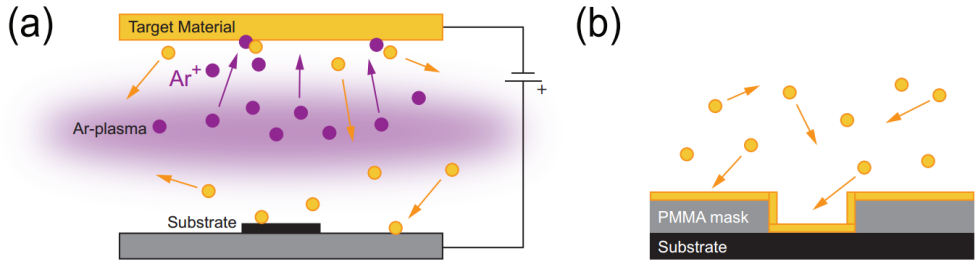

FIGURE 3.1: [11], (a) Illustration of sputtering process. An Argon plasma is created from which the ions accelerate towards a negatively biased target, this will eject target ions, which diffusively hit the target. (b) The diffusive target ions create a homogeneous layer on the substrate.

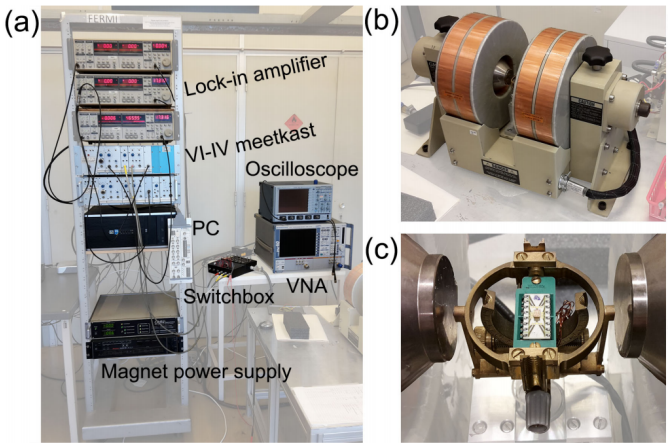

FIGURE 3.2: [11] (a) Picture of the measurement setup, an electronmagnet (b) is also connected to this setup. (c) Rotating sample holder between the two poles of the electromagnet.

3.1.3 Electron-beam Evaporation

Most often Electron-beam Evaporation is used as a controlled deposition method. An electron beam is targetted onto a metal. The electrons will heat up the metal and eventually the target material will start evaporating. This vapor will then rise and deposit on the substrate placed above the material source. The deposition rate is measured by measuring the eigenfrequency of a reference crystal next to the substrate, which can then be calculated to the thickness of the deposited layer.

3.2 Measurement Set-up

The measurements for this thesis are done by rotating a magnetic field from in plane to out of plane with respect to the sample plane. This is achieved yb using an electromagnet, as seen in figure 3.2(b). Between the poles of this electromagnet is a brass rotating sample holder, which is non-magnetic, see figure 3.2(c). In this rotating sample holder sits a 16-pin chip-carrier with the sample bonded on it. The sample holder has 3 degrees of rotation as can be seen in figure 3.3, the first where the sample is tilted, where it is rotated along an angle from y to z. The second can rotate the sample out of plane, so along an angle from x to z and the third will rotate the sample in plane, an angle from x to y which is also the degree of rotation which can be automated by a motor.

A voltage will be sent from the lock-in amplifier to a voltage to current converter. This current amplifier will go to the switchbox where it can be determined which wire on the sample is the injector or the detector and the switchbox can protect the sample by switching the connections on and off when the connections are rewired. The detector

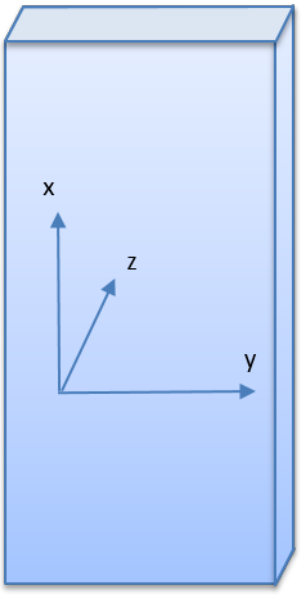

FIGURE 3.3: The sample has three degrees of rotation. It can be rotated along an angle from y to x, from y to z and from x to z

wire is connected to the amplifier of the meetkast which is connected to both the lock-in amplifiers, where the first and second harmonic signal can be separated from each other. All of the measurement equipment is also connected to the computer, from where it is possible to control and automate the measurements.

3.3 Measurement techniques

As mentioned before, the measurements are done using lock-in detection [11]. This technique can differentiate between different order signals of the detected voltage. A voltage with different order signals can be written as

$$V(t) = R_1 I(t) + R_2 I^2(t) + R_3 I^3(t) + \dots \tag{3.1}$$

where R_n is the n-th order response of the system for an applied current $I(t)$. The current used is an AC current and can be written as

$$I(t) = \sqrt{2} I_0 \sin(\omega t) \tag{3.2}$$

where ω is the angular frequency and I_0 the rms of the amplitude of the signal. By knowing the input signal, the lock-in is then able to differentiate between any higher

harmonics. Now the voltage of the n-th harmonic can be written as

$$V_n(t) = \frac{\sqrt{2}}{T} \int_{t-T}^{t} \sin(n\omega s + \phi) V_{in}(s) ds \tag{3.3}$$

where T is the duration of one period and V_{in} is the input voltage form the lock-in amplifier voltage source. Now it´s possible to evaluate this input voltage and obtain the several harmonic responses that correlate with this input voltage. These harmonic voltage signals can then be written as:

$$\begin{aligned} V_1 &= R_1 I_0 + \frac{3}{2} R_3 I_0^3 && \text{for } \phi = 0^\circ \\ V_2 &= \frac{1}{\sqrt{2}} (R_2 I_2^2 + 2 R_4 I_0^4) && \text{for } \phi = -90^\circ \\ V_3 &= -\frac{1}{2} R_3 I_0^3 && \text{for } \phi = 0^\circ \\ V_4 &= -\frac{1}{2\sqrt{2}} R_4 I_0^4 && \text{for } \phi = -90^\circ \end{aligned} \tag{3.4}$$

Now the first and second order response of the system can be written as

$$\begin{aligned} R_1 &= \frac{1}{I_0} (V_1 + 3V_3) \\ R_2 &= \frac{\sqrt{2}}{I_0^2} (V_2 + 4V_4) \end{aligned} \tag{3.5}$$

Now only harmonics up to the fourth harmonic have been taken into account, but this can in principle be extended to even higher harmonics. From equation 3.5 it follows that it is sufficient to study the first and second response of the measurements, since all the higher order signals are present in these responses. These higher harmonics can be extracted by analysing the data, where a fit can be made of the expected signal with respect to the measurement. The difference of the data and the fit, the residual, is the data for the next harmonic response, thus the first residual of the first harmonic response shows the third harmonic signal.

Chapter 4

Results and Discussion

In this chapter the results of the 100 nm YIG will be analyzed and discussed. First the 100 nm thick YIG is compared with 200 nm and 210 nm thick YIG samples from Cornelissen et al. [1] to see the difference in the behaviour of this thinner sample after which the out of plane measurements are analyzed and discussed. The MATLAB code used to process all the data can be found in appendix B.

4.1 Comparison of 100 nm YIG sample with 200 nm YIG samples

The sample that was measured for thesis is based on 100 nm YIG from Matesy, Ukraine. This YIG is thinner and from a different supplier than previous samples measured in the research group [1], therefore some measurements on the sample were taken of which the

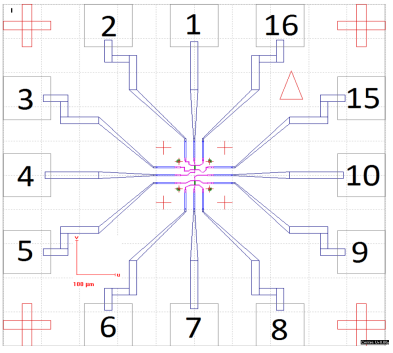

FIGURE 4.1: EBL image of marker field 4 (MF4), the markerfield after fabrication should end up as this one. The blue shapes will form the Ti/Au wires leading from the square labelled pads to the platinum wires, which are the red lines in the middle of the device. The labels on the pads will later be referred to when distinguising a certain platinum wire as either the injector or detector.

results are known for the 200 nm YIG as a way of comparison. The design and sample can be seen in figures 4.1 & 4.2, respectively. The Pt wires, 12500 $nm \times 200\,nm \times 7\,nm$ (l×w×t), were sputtered for 2 seconds. These wires are connected by Ti/Au 5/75 nm thick contacts. Figure 4.2 displays the optical view of one marker field of the sample.

First the local measurements done on the sample will be discussed. When a local measurement is taken, it is meant that the injector and detector is the same strip, a visualization of this can be seen in figure 4.3. In the figure an electron current can be seen going from the source to the electron strip. Here it will excite magnons both thermally and by the SHE. The GGG substrate has approximately the same thermal conductivity as the YIG, so a temperature gradient will go down into the material. The magnon spin current will be parallel to this temperature gradient and since the thickness of the YIG is less than the magnon relaxation length, a magnon spin accumulation will appear at the interfaces with opposite signs between the YIG|GGG- and Pt|YIG interface [1]. The magnons at the Pt|YIG interface will then by virtue of spin pumping be absorbed by the platinum wire leaving a spin-polarized asymmetry in the detector strip, which in turn will induce a current by virtue of the ISHE.

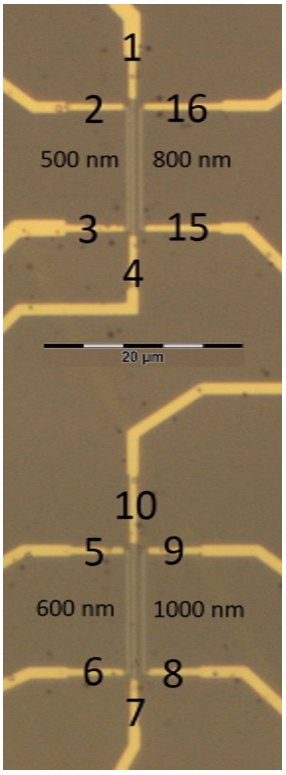

FIGURE 4.2: Optical image of MF4 made on top of 100 nm YIG from Ukraine, Matesy. The Pt wires, 12500 $nm \times 200\,nm \times 7\,nm$ (l×w×t), were sputtered for 2 seconds and can be seen in the figure as the lighter green wires between the numbered gold wires. These wires are connected by Ti/Au 5/75 nm thick contacts. The terminals to which the contacts are connected are labelled appropriately in the image. The distances between each of the Pt wires is from centre to centre.

4.1.1 Spin Magneto Resistance

The Spin Magnetoresistance (SMR) can be obtained from the local measurement by two ways. The first is by doing an angle sweep at fixed magnetic field as can be seen in figures 4.5 & 4.6. In this measurement the angle between the polarization direction of the spin-polarized current and the magnetization of the YIG will vary. By following the right-hand-rule in section 2.2.1.2 it can be deduced that a spin-polarized current with spin-polarization antiparallel with B at 0 degrees will be at the Pt|YIG interface, see figure 4.5. When the magnetization is perpendicular to the strip, it will be parallel to the spin polarization direction, as is the case for $\alpha = 0$, thus the angular momentum of the electron will not be transferred to the YIG, as can also be understood from 2.10. The electron will then reflect from the Pt|YIG surface and will keep their spin-polarization. This spin-current will then flow back into the platinum. This spin-current will create a charge current according to the ISHE which will be in the same direction as the current from the source. Therefore, the same current that was sent will be detected, thus a maximum should be expected here. If magnetization is parallel to the strip, so perpendicular to the spin-polarization, then the angular momentum of the spin-polarized electrons will mostly be absorbed by the YIG. These magnons will dissipate in the material and only the sent charge current will be detected, thus a minimum should be expected here [11]. The result of such a measurement can be seen in figures 4.5 & 4.6. The SMR from these plots can be calculated as:

$$\Delta R/R = SMR \tag{4.1}$$

and the results are displayed in table 4.1. The values of these signals come in close agreement with the ones in figure 4.4, which is a plot of the SMR signal to platinum thickness.

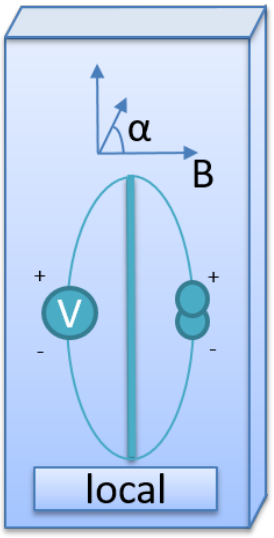

FIGURE 4.3: Example configuration for a local measurement

The platinum that was sputtered is approximately $7\,nm$ thick, which corresponds to an SMR of $SMR \sim 2E-4$. In the result for strip 5-6 it can be seen that there is some negative drift in the curve, this is not present for the SMR curve for strip 7-10. The reason for this drift could be that as time increases the platinum strip will heat up and the resistance will lower, thus explaining the slope since the measurements are started at -360 degrees. Strip 7-10 is already warmed up more, since the total resistance is already much smaller than for strip 5-6 and consequently no clear negative slope can be seen in this signal. Since the SMR signal for $100\,nm$ YIG is in close agreement with the SMR signal for $200\,nm$ YIG it can be concluded that the thinner YIG has no clear effect on the SMR, which makes sense, since the SMR is only dependent on the spin-mixing conductance of the Pt|YIG interface.

The second way to measure the SMR signal is by doing a magnetic field sweep on a sample where the magnetic field is perpendicular on the injector and detector. Here a peak or dip should be seen in the resistance of the detector when the magnetic field passes the value for the coercive field H_c, which would be around $1.25E-4\,T$. The reason for this is as the magnetic field passes the coercive field, the magnetization will briefly be perpendicular to the spin-polarization direction and thus most of the angular momentum of the spin-polarized electrons will be absorbed by the YIG. The result for this measurement can be seen in figure 4.7. The top graph shows this peak. The blue

Strip	SMR
5-6	1.566E-4
7-10	2.047E-4

TABLE 4.1: SMR values based on local measurements of the first harmonic obtained from figures 4.5 & 4.6. Platinum thickness of the strips is $\sim 7\,nm$

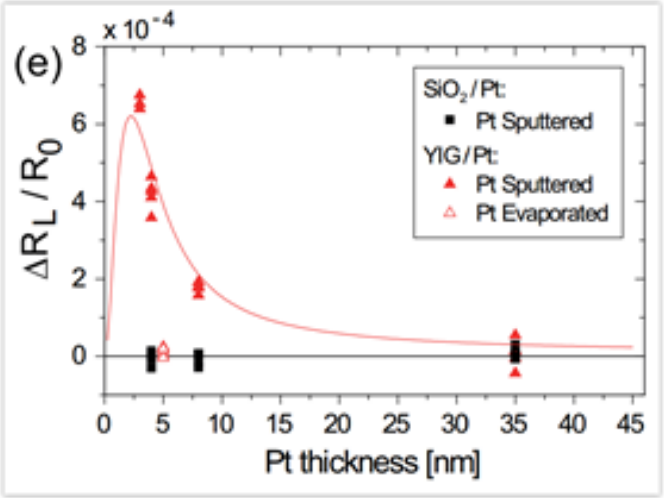

FIGURE 4.4: SMR magnitude as a function of thickness of the platinum, taken from Vlietstra [11]

part of the graph is the trace and the red part the retrace. The reason why no peak is shown in the red part can be due to the fact that this type of measurement has a low resolution, so it is possible that the peak is skipped by one increasing step of the magnetic field, since the smallest stepsize is $0.4\,mT$. The reason why the red part decreases as the measurement continues is that the current going through the injector and detector strip will heat the strip, therefore decreasing the resistance of it. The peak of this measurement was measured to be $248\,m\Omega$. Taking the strip resistance this comes to an SMR for strip 8-9 of $SMR = 0.69E-4$. This value is however much lower than the previous SMR measurement, which once again may be due to the low resolution of this type of measurement.

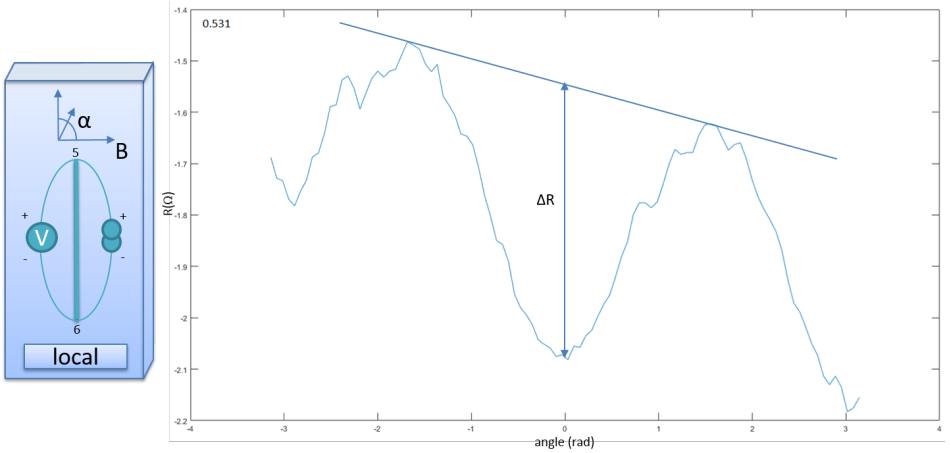

FIGURE 4.5: In plane measurement on the first harmonic local signal, $5\,mT$, $200\,\mu A$, I+5, I-6, V+5, V-6, V-I- on ground. The resistance of the strip is $3.39\,k\Omega$ and from the graph $\Delta R = 0.531\,\Omega$ can be obtained, which gives $SMR = 1.566E-4$. A negative sign at $\alpha = 0$ is observed.

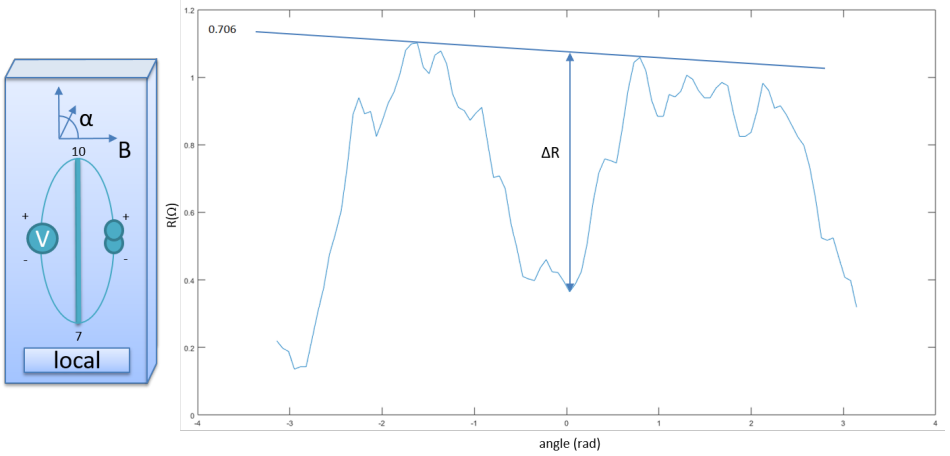

FIGURE 4.6: In plane measurement on the first harmonic local signal, $5\,mT$, $200\,\mu A$, I+10, I-7, V+10, V-7, V-I- on ground. The resistance of the strip is $3.45\,k\Omega$ and from the graph $\Delta R = 0.706\,\Omega$ can be obtained, which gives $SMR = 2.047E-4$. A negative sign at $\alpha = 0$ is observed.

4.1.2 Local Spin Seebeck voltage in the second harmonic signal

Some of the thermal characteristics of the thinner YIG can be determined by comparing the local second harmonic measurements with previously reported results [1]. Since the YIG is thinner and smaller than the magnon relaxation length there would be a magnon spin accumulation at the YIG|GGG and Pt|YIG interfaces with opposite signs. Therefore the signal from the second harmonic should not be affected too much by the thickness of the YIG, just by the current sent through. The results for this measurement can be found in figures 4.8 & 4.9. Cornelissen et al. [1] reports a magnitude of $2E-5\,V$ for the local second harmonic signal, which is approximately the same magnitude of the result on strip 5-6. This also agrees nicely with the result previously obtained for the first harmonic local signal, where strip 5-6 had a similar SMR to the one reported for $200\,nm$ YIG and again the signal is a little bit smaller. Strip 7-10 however has a SSE voltage which is about 4 times smaller than for the thicker YIG, which is quite curious considering the resistances of both strips are approximately the same and the current sent through both strips is the same. The signal from the measurement of strip 7-10 itself is already 4 times smaller than the signal for strip 5-6, therefore the voltage of the measured signal should also be 4 times smaller than for strip 5-6. This could imply that either the

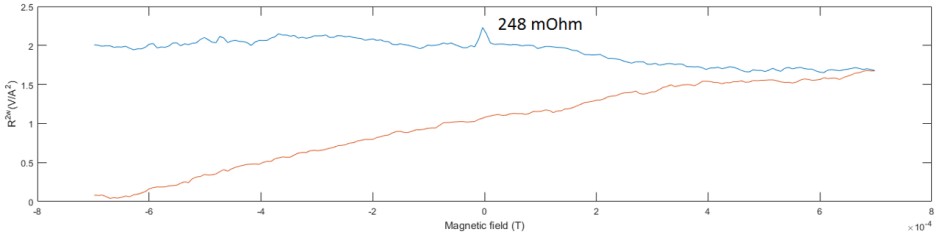

FIGURE 4.7: In plane measurement with fixed angle and variable magnetic field at $200\,\mu A$, I+8, I-9, V+8, V-9. V-I- on ground. The strip resistance is $3.58\,k\Omega$ and from the graph $\Delta R = 0.248\,\Omega$ can be obtained, which gives $SMR = 0.69E-4$.

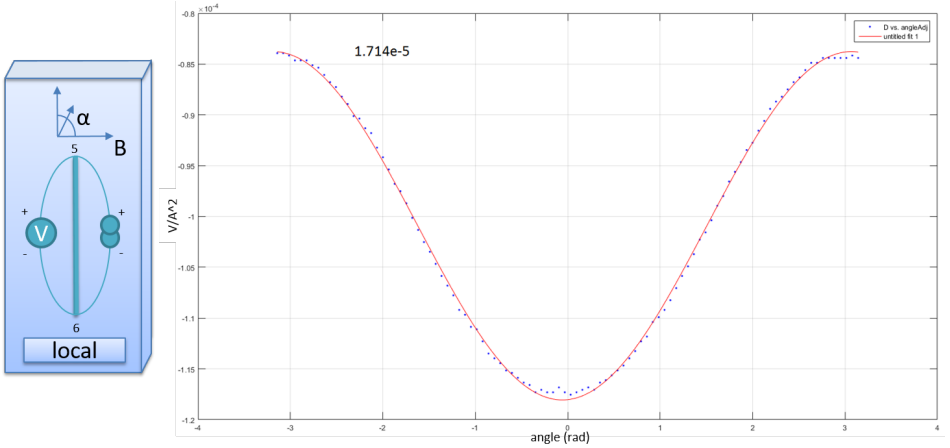

FIGURE 4.8: In plane measurement on the second harmonic local signal, $5\,mT$, $200\,\mu A$, I+5, I-6, V+5, V-6, V-I- on ground. Amplitude of the signal is $1.714E-5\,V$.

wiring during that measurement was defect or that the resistance of the strip itself had changed due to annealing effects. While the resistance of that strip did indeed change after some measurements it did not return a resistance 4 times lower. As for the shape, the non-equilibrium magnons created by the joule heating have a magnetic momentum opposite of the magnetization, so antiparallel to B at $\alpha = 0$ in figure 4.8. As described in section 1.2 the magnons transport diffusive through the YIG and will accumulate at the GGG|YIG interface. This causes a magnon gradient where magnons with an opposite magnetic momentum will accumulate at the PT|YIG interface, so parallel to B at $\alpha = 0$. Because of the spin pumping an electron with spin-polarization opposite to the magnetic momentum will be excited at the Pt|YIG interface, so antiparallel to B at $\alpha = 0$. The electron propagation direction and the spin-polarization directions are known, then by virtue of the sign of the ISHE the electron deflection is in the direction towards V+7, thus a minimum should be expected at 0 degrees. This sign is consistent with the one observed by Cornelissen et al. [1]. To conclude, the measurement on strip 5-6 does confirm the hypothesis that the local SSE signal of the second harmonic should not differ for thinner YIG.

4.1.3 Magnetization of the YIG

The $100\,nm$ YIG will have different magnetization properties than its $200\,nm$ thick counterpart. Because the material is thinner it will cost more energy to align the magnetization of the YIG out of plane since it is easier for the $100\,nm$ YIG to have its magnetization in plane, the easy axis and because of the shape anisotropy of the YIG, which is even more anisotropic since the YIG is smaller, the magnetization will be even

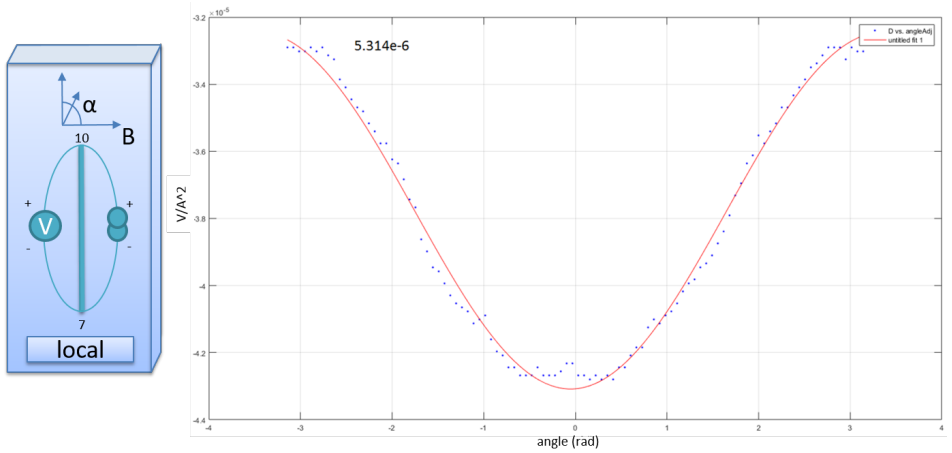

FIGURE 4.9: In plane measurement on the first harmonic local signal, $5\,mT$, $200\,\mu A$, I+10, I-7, V+10, V-7, V-I- on ground. Amplitude of the signal is $0.5314E-5\,V$. The electrons go towards V+10 thus the current detected has opposite sign from the current source, thus the positive maximum at 0 degree should be a negative minimum, as can be seen.

more difficult to pull out of plane. This will also have an effect on the coercive field for in plane magnetic field sweeps. In figure 4.10 the in plane magnetization for a local measurement can be seen and in figure 4.11 the magnetization for 45 degrees out of plane magnetization. A clear hysteresis loop can be seen in both figures. From the in plane measurement the coercive field is determined to be $H_c = 1.25E-4T$, while the coercive field for the 200 nm YIG is $0.6E-4T$ [11], so the coercive field for 100 nm YIG is approximately twice as large for in plane magnetization.

Figure 4.11 shows the magnetization curve for YIG that is 45 degrees out of plane. Around zero the hysteresis curve for in plane magnetization can still be seen, however the slope at higher magnetic fields indicates that the out of plane component of the YIG

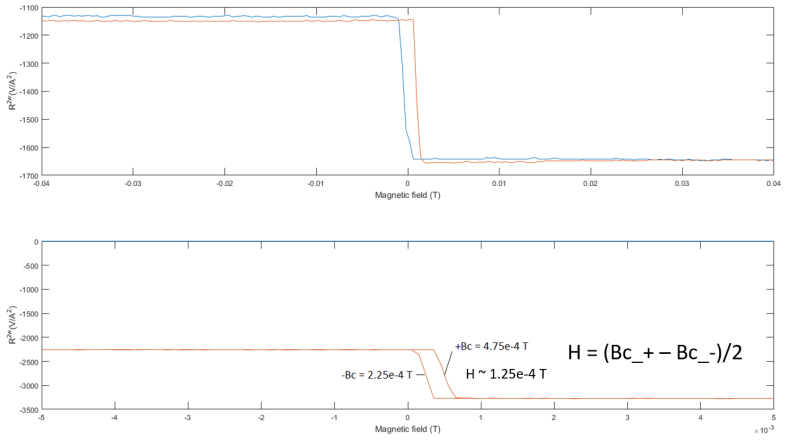

FIGURE 4.10: Coercive field for in plane 100 nm thick YIG, 200 μA, I+8, I-9, V+8, V-9, V-I- on ground.

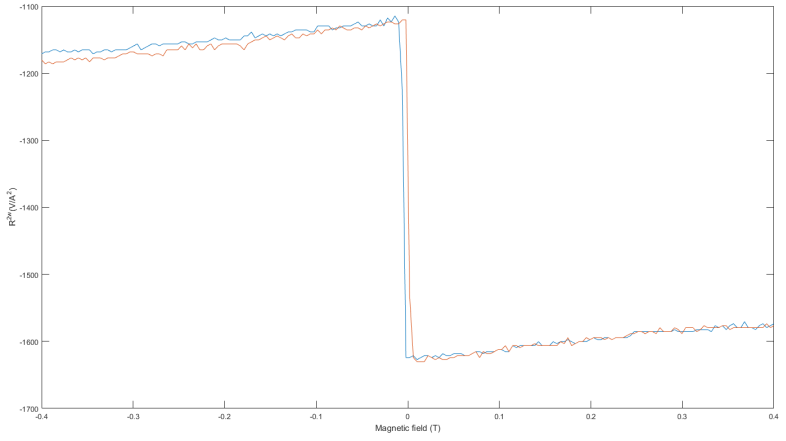

FIGURE 4.11: Coercive field for in plane 100 nm thick YIG, 200 μA, I+8, I-9, V+8, V-9, V-I- on ground. The resistance as a function of magnetic field is shown. H is the coercive field and Bc_+ and Bc_- two points on the hystersis loop chosen at the same resistance to help determine the coercive field.

is not completely saturated yet. Therefore any out of plane measurement taken will not be completely saturated, since the measurement setup did not allow any higher magnetic fields. However, the Stoner Wholfarth model 2.6 can still be applied, so this will not prove to be a problem when analyzing the results.

4.1.4 Nonlocal in plane measurements

To see if the magnon transport is different for the 100 nm YIG some nonlocal in plane measurements are done. The thinner YIG may behave different due to the spin accumulation at the YIG|GGG interface having a higher reach. As Cornelissen et al. [1] reported for 200 nm YIG, nonlocal measurements up to 500 nm showed a change of sign due to the spin accumulation at the YIG|GGG interface having the same effect for local as for these nonlocal measurements. The measurements can be seen in figures 4.12-4.17.

4.1.4.1 Shape of the non-local measurements

First of all the shape of the second harmonic signals can be explained as follow, where figure 4.12 will be taken as example. The magnetic moment of the thermal non-equilibrium magnons will be opposite to the magnetization of the material, so antiparallel to B at $\alpha = 0$. The magnons will diffuse and some of them will get picked up by the detector strip, here the magnons will excite electrons with a spin-polarization direction opposite to the magnetic momentum of the magnon. So the electrons in the detector have a spin-polarization parallel to B at $\alpha = 0$. Because of the detection efficiency, where only the electrons with spin-polarization perpendicular to the detector strip will be measured due

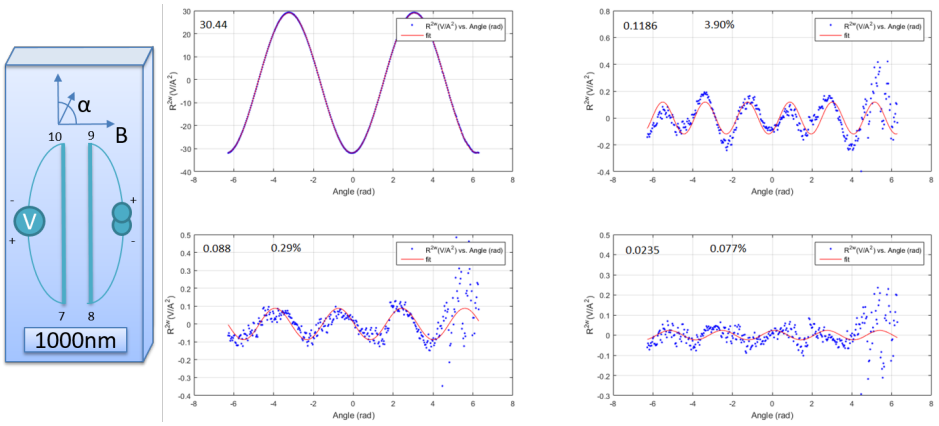

FIGURE 4.12: In plane magnetic field measurement second harmonic for 1000 nm injector detector distance, $B = 40\,mT$, $600\,\mu A$, I+9, I-8, V+7, V-10, V-I- on ground. The top left graph is the signal and a sine function fit on that signal, the top right graph is the residual of the first, again with a sine fit, the bottom left graph is the residual of that graph and its fit and finally the bottom right graph is again the residual.

to the ISHE, a $cos(\alpha)$ dependence should be expected. Now the propagation direction of the electron and the spin-polarization direction is known and by using this with the right hand rule for ISHE from section 2.2.1.2, the electron will deflect to V=7 for B at $\alpha = 0$. Therefore a positive or negative maximum of the signal will be present each time the field is perpendicular to the detector strip. Now by definition of the voltage where the voltage is positive if the negative charge flows towards the negative pole, a minimum signal should be expected since the electrons travels towards V+7 for B at $\alpha = 0$. This is also what can be seen in figure 4.12.

The shape for the first harmonic measurements is different from the second harmonic as will be explained with figure 4.13 as example. The electrons start from the negative side of the current source and travel through the injector where they will deflect according to the SHE. A spin-polarized current in with polarization direction antiparallel to B at $\alpha = 0$ is deflected toward the Pt|YIG interface. From the spin-mixing conductance explained in 4.1.1 it is known that if the applied magnetic field is perpendicular to the injector strip most of the angular momentum of the electrons get absorbed by the YIG where their magnitude is $cos(\alpha)$ dependent. The magnetic moment of the magnons generated by this current will be in opposite direction of the spin-polarization direction, so parallel to B at $\alpha = 0$. The magnons will then travel diffusive and some get picked up by the detector strip. As explained for the second harmonic, because of the detection efficiency, where only the electrons with spin-polarization perpendicular to the detector strip will be measured due to the ISHE, a $cos(\alpha)$ dependence should be expected, so antiparallel to B at $\alpha = 0$. Again the propagation direction of the electron and the spin-polarization direction of the electron is known, so by using the right-hand-rule for

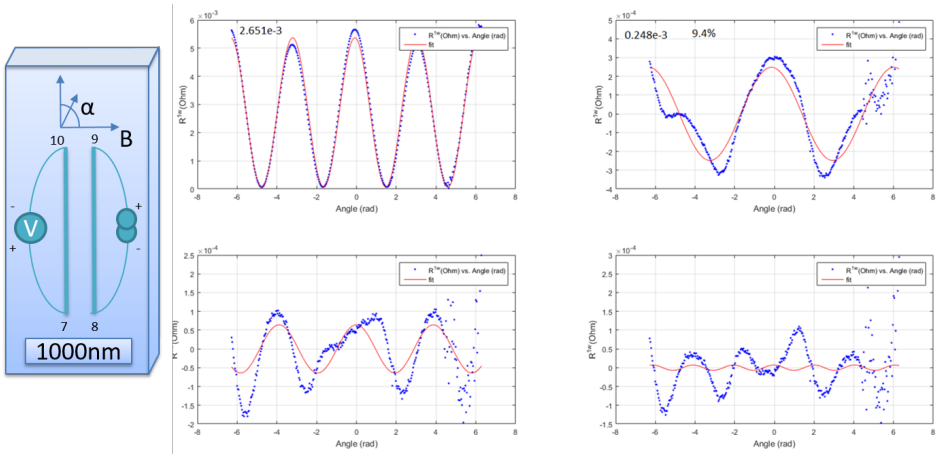

FIGURE 4.13: In plane magnetic field measurement first harmonic for 1000 nm injector detector distance, $B = 40\,mT$, $600\,\mu A$, I+9, I-8, V+7, V-10, V-I- on ground. The top left graph is the signal and a sine function fit on that signal, the top right graph is the residual of the first, again with a sine fit, the bottom left graph is the residual of that graph and its fit and finally the bottom right graph is again the residual.

the ISHE from section 2.2.1.2 the electrons are deflected towards V-10. Therefore a maximum should be expected every 180 degrees. This is also what can be seen in figure 4.13

In figure 4.13 a pi asymmetry can be seen which cannot be explained from the SHE and ISHE. This pi asymmetry is an artifact from the measurement setup. The AC current generated by the amplifier has a small DC component so that

$$I = I_{DC} + I_0 sin(\omega t) \tag{4.2}$$

Now because of the quadratic current dependence of the second harmonic signal

$$I^{2\omega} \propto I^2 \tag{4.3}$$

$$I^{2\omega} \propto I_{DC}^2 + I_0^2 sin^2(\omega t) + 2 I_{DC} I_0 sin(\omega t) \tag{4.4}$$

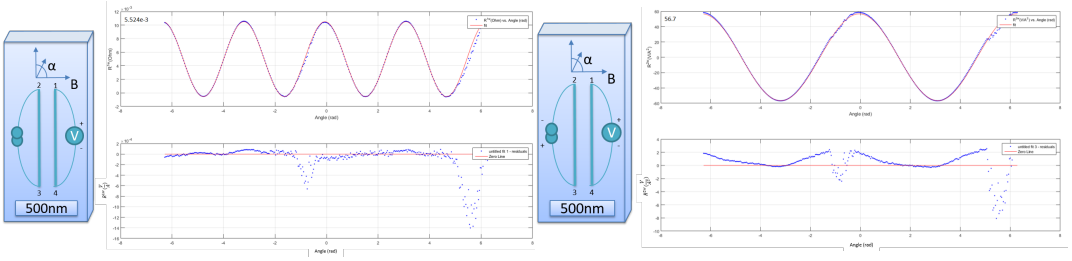

FIGURE 4.14: In plane magnetic field measurement first harmonic for 500 nm injector detector distance, $B = 40\,mT$, $200\,\mu A$, I+3, I-2, V+1, V-4, V-I- on ground. The top graph is the measurement and a sinusoidal fit with fixed period of π and the bottom graph is the residual.

FIGURE 4.15: In plane magnetic field measurement second harmonic for 500 nm injector detector distance, $B = 40\,mT$, $200\,\mu A$, I+3, I-2, V+1, V-4, V-I- on ground. The top graph is the measurement and a sinusoidal fit with fixed period of π and the bottom graph is the residual.

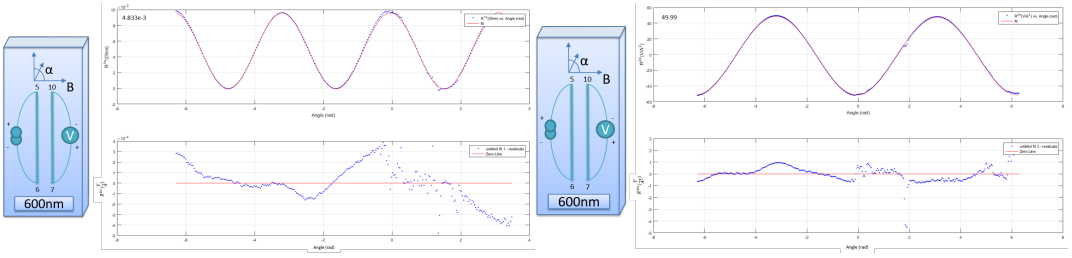

FIGURE 4.16: In plane magnetic field measurement first harmonic for 600 nm injector detector distance, $B = 40\,mT$, $500\,\mu A$, I+5, I-6, V+7, V-10, V-I- on ground. The top graph is the measurement and a sinusoidal fit with fixed period of π and the bottom graph is the residual.

FIGURE 4.17: In plane magnetic field measurement second harmonic for 600 nm injector detector distance, $B = 40\,mT$, $500\,\mu A$, I+5, I-6, V+7, V-10, V-I- on ground. The top graph is the measurement and a sinusoidal fit with fixed period of π and the bottom graph is the residual.

The last term on the right-hand part will arise in the first harmonic signal, therefore a DC component is measured in the first harmonic, as can be seen from the measurement data. Even though the DC component is small it does have an influence on the measurements because the signal measured is also small. The pi asymmetry is then due to this DC component having a $sin(\omega t)$ dependence.

With these in plane measurements it is possible characterize the signal to distance dependence as can be seen in figures 4.18 & 4.19. Comparing these with previously reported signal to distance measurements [1] shows that the values for the first harmonic signal are similar to the previously reported measurements, albeit slightly larger. The second harmonic signal however is approximately twice as small. Since these are the thermal magnons it is possible that the magnon gradient is smaller compared with the 200 nm YIG, since less magnons will be able to pile up at the bottom of the YIG, as is the case for the local second harmonic signal.

4.2 Out of plane measurements

Following the hypotheses made in section 2.4.3 out of plane measurements are done, so that if there is an AHE for magnons in YIG it should be seen from these measurements. The results for the out of plane measurements can be seen in figures 4.20 & 4.21, where the magnetic field sweeps from in plane to out of plane whilst always being perpendicular to the injector and detector strips. Also since no qualitative or quantitative has been made yet, the strategy of obtaining some result is to analyze the results and check all the signals if they are artifacts from the measurement setup so that these can be removed.

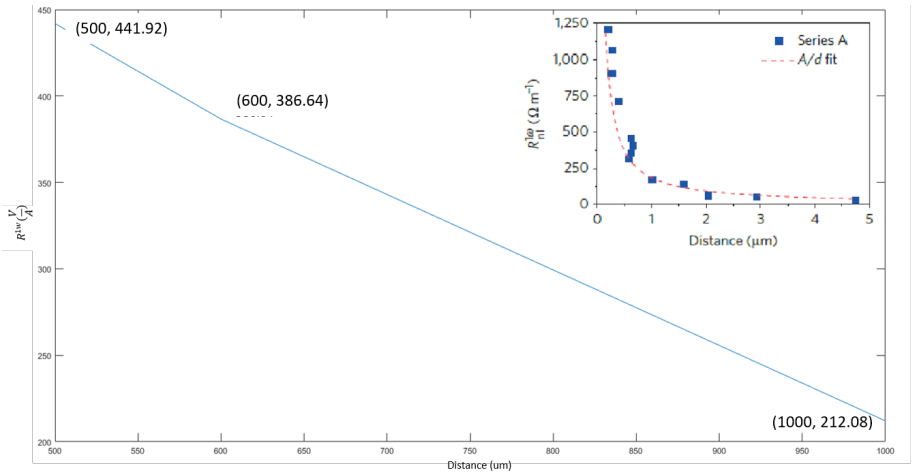

FIGURE 4.18: Magnitude of the first harmonic signal for in plane measurements at several nonlocal distances for various currents and 40 mT

First the second harmonic signal will be discussed, which can be seen in figure 4.21. The shape of the signal can be explained in the same way as was done in section 4.1.4.1. Furthermore from the residual plots from figure 4.21 three signals can be seen apart from the measured signal, each signal having some 2-fold component added to it. If there would be an AHE for magnons it should be one these signals. The discussion of these signals will continue in section 4.2.1.

The first harmonic signal can be seen in figure 4.21. Again the shape can be explained

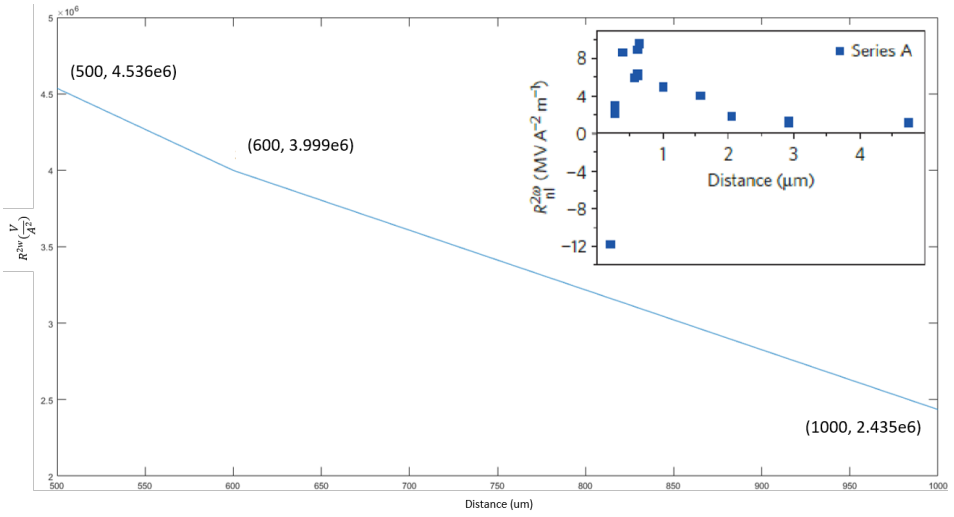

FIGURE 4.19: Magnitude of the second harmonic signal for in plane measurements at several nonlocal distances for various currents and $40\,mT$

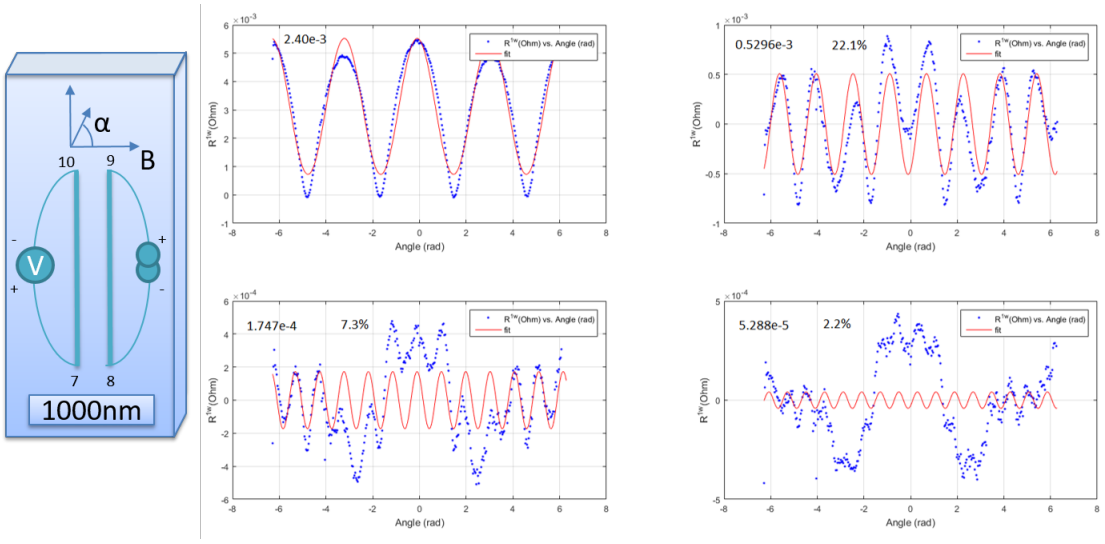

FIGURE 4.20: First harmonic signal for out of plane measurements, $B = 350\,mT$, $600\,\mu A$, I+9, I-8, V+7, V-10, V-I- on ground. Nonlocal measurement with $1000\,nm$ injector-detector spacing. The top left graph is the signal and a sine function fit on that signal, the top right graph is the residual of the first, again with a sine fit, the bottom left graph is the residual of that graph and its fit and finally the bottom right graph is again the residual. The number in the plot is the magnitude of the signal and how large this signal is compared to the total measured signal.

in the same way as done in section 4.1.4.1. Two clear signals can be seen in the residuals from figure 4.20 each adding a 2-fold component, the last residual is too noisy to really use.

4.2.1 Stoner Wohlfarth model

As discussed in section 2.6 the magnetization of an anisotropic material does not completely follow an applied magnetic field if this field is varied with angle and if the applied magnetic field is not large enough. The model shown in that section can be applied to the measurements, where the angle of the magnetic field is replaced by the angle of the magnetization. Doing this process results in figures 4.22 & 4.23. Now the measurements with and without the Stoner Wholfarth model applied can be compared with each other. First of all the signal looks much more like the one seen for the in plane measurements for both harmonics, the sharp corners at 90 degrees for the first harmonic are gone and the second harmonic signal is less rounded. The curves are still not entirely the same, due to some other out of plane magnetization physics, therefore a small signal due to this magnetization lagging should still be present, albeit considerably smaller.

For both the second and first harmonic signal, figure 4.23 and 4.22 it can be seen that the second residual signal from the original measurement compares with sign and magnitude with the first residual signal from the measurement with SW model applied. The

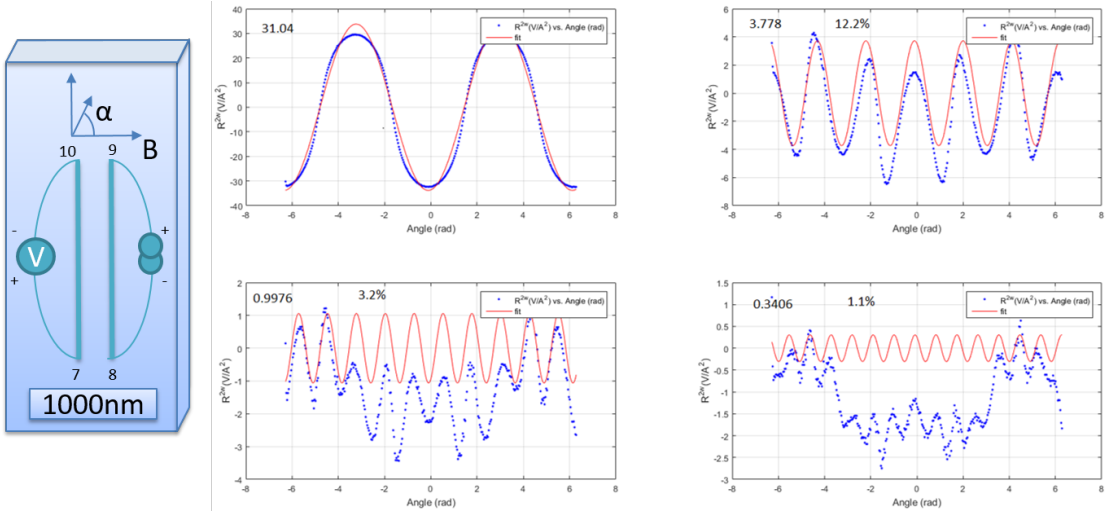

FIGURE 4.21: Second harmonic signal for out of plane measurement, $B = 350\,mT$, $600\,\mu A$, I+9, I-8, V+7, V-10, V-I- on ground. Nonlocal measurement with $1000\,nm$ injector-detector spacing. The top left graph is the signal and a sine function fit on that signal, the top right graph is the residual of the first, again with a sine fit, the bottom left graph is the residual of that graph and its fit and finally the bottom right graph is again the residual. The number in the plot is the magnitude of the signal and how large this signal is compared to the total measured signal.

same observation is also true when comparing the third residual signal from the original measurement with the second residual signal from the measurement with SW model applied. Also in the third residual signal of both measurements with SW model applied a pi-asymmetry can be seen, which was not obvious previously. The pi-asymmetry of the first harmonic is due to the same reasons there was a pi-asymmetry in the non-local in plane measurements. The pi-asymmetry in the second harmonic signal however has a -90 degrees phase shift when compared with the pi-asymmetry of the first harmonic signal, but the same reasoning does not apply here.

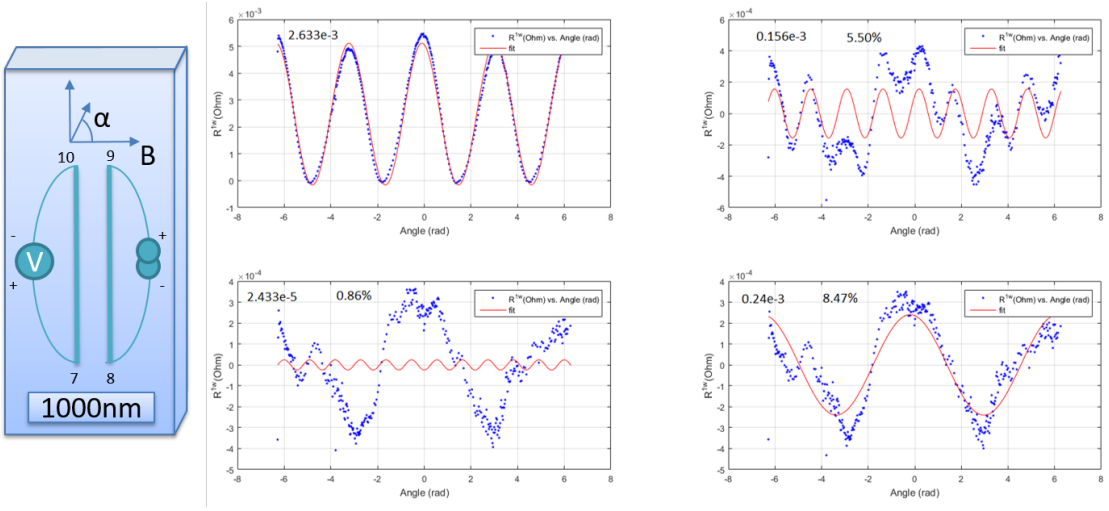

FIGURE 4.22: Measurement data of figure 4.20 adjusted according to the Stoner Wholfarth model. 90 degrees out of plane first harmonic signal, $350\,mT$, $600\,\mu A$, I+9, I-8, V+7, V-10, V-I- on ground. Nonlocal measurement with $1000\,nm$ injector-detector spacing. The number in the plot is the magnitude of the signal and how large this signal is compared to the total measured signal.

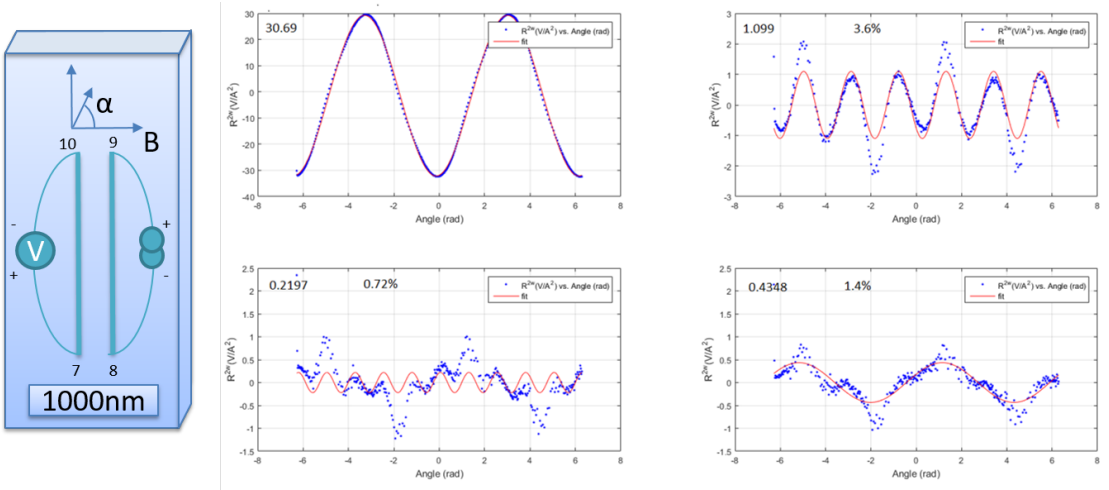

FIGURE 4.23: Measurement data of figure 4.21 adjusted according to the Stoner Wholfarth model. 90 degrees out of plane second harmonic signal, $350\,mT$, $600\,\mu A$, I+9, I-8, V+7, V-10, V-I- on ground. Nonlocal measurement with $1000\,nm$ injector-detector spacing. The number in the plot is the magnitude of the signal and how large this signal is compared to the total measured signal.

4.2.2 Comparison of the hypotheses for the AHE for magnons with the measurement data

As was discussed in section 2.4.3 the anomalous Hall effect for magnons should have an opposite sign for magnons with opposite magnetic momentum. Furthermore, this AHE for magnons should be maximum when the magnetic field is orthogonal to the direction of the magnon spin current and the magnetic moment of the magnon. This would mean that the AHE for magnons should appear in the out of plane measurements as some signal, which should be maximum at $\alpha = 0.5\pi + n\pi$ degrees and zero when $\alpha = 0 + n\pi$ degrees. This magnon should then show some 1-fold behaviour.

Now if the AHE for magnons should be observed in the second harmonic signal, then this AHE is also subject to the detection efficiency, therefore, the AHE for magnons for the second harmonic measurement should show as some 2-fold signal. However, when looking at figure 4.23 only a 3-fold and 5-fold signal can be seen, therefore the AHE for magnons was not observed in the second harmonic signal.

If the AHE for magnons should be observed from the first harmonic measurement, then this AHE is subject to both the injection and detection efficiecy, therefore it should show as some 3-fold signal. When looking at figure 4.22 only a 4-fold and 6-fold signal can be observed, therefore the AHE for magnons cannot be seen in the first harmonic signal

Chapter 5

Conclusion

From the comparison of the SMR signal for $100\,nm$ thick YIG and $200\,nm$ thick YIG it was observed that the SMR signal did not change for the thinner YIG, which can be explained due to the fact that the SMR is a parameter which is dependent on the spin-mixing conductance of the Pt|YIG interface. This interface is not affected by the thickness of the YIG, therefore the SMR is the same for both measurements.

From the local SSE voltage in the second harmonic it was observed that one of the signals was of equal magnitude compared with [1], which would suggest that the magnitude of the local SSE signal for the second harmonic is not dependent on the thickness of the YIG. It is known that the magnon gradient of the local SSE measurements is dependent on the thickness of the YIG, because if the thickness would be greater than the spin relaxation length of the magnon, then a sign change would be observed [1]. However the YIG was still smaller than the magnon spin relaxation length, thus the sign stayed the same, as was observed.

The coercive field of the $100\,nm$ thick YIG was observed to be twice as big than for $200\,nm$ thick YIG, this would mean that the shape anisotropy effects have a bigger magnitude for the thinner YIG. This would then explain that it is more difficult to change the magnetization from the YIG from parallel to anti-parallel magnetization. From the measurement with an applied magnetic field at an 45 degree angle with a field strength twice as big as the out of plane saturation magnetization for $200\,nm$ thick YIG, which is $176\,mT$ [11], it was observed that the $100\,nm$ thick was not fully saturated yet.

The non-local in plane measurements showed that the sign as expected for $200\,nm$ thick YIG was still the same. Thus the thinner YIG does not seem to have an influence on the sign when compared with the $200\,nm$ thick YIG. From the signal to distance ratio of the in plane measurements it can be concluded that the thinner YIG does not have

an effect on the first harmonic signal. For the second harmonic signal however it can be observed that the magnitude of the signal is half as large when compared with the $200\,nm$ thick YIG. This would mean that the thinner YIG has influence on the transport of the thermal magnons. It could be possible that more of the heat is dissipated through the surface of the YIG, thus that the thermal magnons would relax faster.

From the out of plane measurements it was seen that the SW model had influence on the measurements. Since the second and third residual of both harmonics from the original measurement data correspond with magnitude and sign with the first and second residual of both harmonic, respectively, from the data with SW model applied, it can be concluded that the first residual data from the original measurements is the signal due to the SW model.

It is possible that some of the residual signals left in figures 4.23 and 4.22 are also due to artifacts of the measurement setup. One of these artifacts could be the Anisotropic Magnetoresistance, where the resistance of the magnon travel path is dependent on the anisotropy of the crystal structure.

The AHE for magnons was not observed in both harmonic signals. One reason could be that the AHE for magnons is subject of a bulk effect, just like the skew-scattering and side-jump contribution of the AHE for electrons, which are dependent on the chirality and impurities of the material, respectively. Since the YIG is so small it is possible that the contributions from impurities and chirality are so small that they are not measured in this kind of measurement setup, since the AHE for magnons would be on the same magnitude as the noise measured. What is also possible is that the device geometry is not suitable for measuring the AHE for magnons even though the magnons transport diffusive.

Appendix A

Device Fabrication Steps

The fabrication of each device starts the same. A layer of 100nm thick YIG is grown onto the (111) plane of a [thick] layer of $Gd_3Ga_5O_{12}$ by [method]. From this wafer a small piece is cut off and that will be the basis of the device fabrication.

A.1 Cleaning of the Sample

The cleaning procedure is as follows:

1. First dip the sample into de-ionized H_2O to get some initial dirt off.
2. Now put the sample into 45 °C acetone for approximately 5 minutes and then place the beaker of acetone with the sample in it directly into a sonicator and let it sonicate for 30 seconds at power 9.
3. Rinse the sample with isopropanol (IPA) for 30 seconds and after finishing also rinse it with ethanol for 30 seconds to clean off almost all dirt.
4. Dip it into de-ionized H_2O again to wash off the ethkanol and blow dry it with a nitrogen-gun.
5. Finally bake it for 30 seconds at 180 °C to remove all remaining water residue.

Now the sample has been cleaned and can be checked under the optical microscope to see if most if not all of the dirt is gone. If there is still some left, then steps 2-5 can be repeated again.

A.2 Spin Coating

The spincoating is done as following:

1. Take a chuck which fits with the spincoating machine and place the sample centered as much as possible on the hole in the chuck, also make sure the hole is sufficiently small to prevent any liquid being sucked into the hole. Now place the chuck into the spincoating device. Press 'Vac' to engage suction.
2. Select or create a spinning recipe which is set to 4000 rpm for 60 seconds. This setting is applicable to 2%, 3% and 4% PMMA.
3. Prepare a hotplate recipe at 180 °C for 90 seconds, which will be used after the spincoating is done.
4. Take a small amount of PMMA in a pipet and deposit a few drops next to the chuck before placing a droplet onto the sample. Make sure it is large enough without falling of the sample. If everything went well, the droplet will remain unmoved on the sample.
5. Now the spincoating device can be closed and turned on.
6. After it´s done place the sample on the heated hotplate and let the program run.
7. If the sample is done heating take a look at it under an optical microscope. If the PMMA-layer is uniform on the device, besides the edges, then we can continue, otherwise clean the sample and repeat the previous steps (be aware not to turn up the sonication power too high if there are already structures on the sample)

After this is done the sample is checked under the optical microscope to see if everything is alright, if the surface is uniform enough. If this is the case we can proceed with the EBL itself.

A.3 EBL Procedure

The following steps for EBL were done:

1. Load the sample into the loading stage after the EBL-machine is done venting. To make it easier to pattern, the sample is put mostly parallel to the edges of the loading stage and the sample is clamped on some non-homogeneous side of the sample to the loading stage. If the sample is in place, click the load sample button

and then the EBL-machine can start pumping to reach vacuum again. Check if the desired pressure is reached before continuing the procedure.

2. Now the beam current and size of aperture must be chosen. However the beam current can vary slightly so it needs to be measured and the beam will also be out of focus. To measure the beam current, the beam is targeted onto the middle of the hole of the Faraday cup on the loading stage and after letting it stabilize the current can be read from the program. Based on the measured current the dwell time can be determined for a specified step size and electric flux density. Now there is a test sample (Si/SiO_2) on the loading stage as well which can be used to align the beam to the write field to prevent the sample of interest from being overexposed due to aligning the beam. The beam is aligned to the write field for multiple areas reducing in size. The beam is then angled a bit from four sides which is then calibrated to make sure the beam is circular when hitting the sample. Finally focus wobble is done to tune the focus of the beam some more. The beam is now calibrated.

3. To make sure where on the sample the beam will pattern a 3-point alignment needs to be done first. Making sure that the beam is exposing a small area, three corners of one sample can be targeted and on each corner the (u,v) coordinate can be set, with the bottom left corner as (0,0). After setting a (u,v) coordinate it is important to read the (x,y) coordinate and to adjust it.

4. From the three coordinates it can be determined how big the area of the sample is which can be used to determine how many marker fields fit onto the sample, where each marker field is (1000 μm x 1000 μm) in size. Making sure that these fields are at least 500 μm away from the edge of the sample and at least 200 μm away from each marker field, the marker fields can be patterned. Start with creating a position-list and then the pattern for the marker can be selected from a layer from the E-Line design of the device.

A.4 Development

The development process was done as follows:

1. First wash away the aquaSAVE with some de-ionized H_2O for 30 seconds.

2. Now the short chain polymers can be developed and washed away by first holding the sample in MIBK:IPA (3:1), where MIBK is methyl isobutyl ketone, for 30

seconds and then immediately holding the sample in IPA for 30 seconds to stop the development, otherwise the long chain polymers would also go away.

3. Spin dry the sample for another 30 seconds at [amount] rpm. Now the mask can be looked at one final time under the optical microscope to see if the mask is correct or not.

After the development is done we can deposit some material on the sample by ways of sputtering or evaporation. For the samples that were created the Pt wires were sputtered and the Ti/Au contacts were evaporated.

A.5 Lift-off

The lift-off was done as follows.

1. Prepare two beakers of 45 °C acetone during the deposition.
2. Place the sample in one beaker of 45 °C acetone and let it rest for approximately 15 minutes.
3. Take the beaker of acetone with the sample in it and carefully take some of the hot acetone with a pipet. Place the pipet into the acetone with the sample in it and gently blow on your sample from the top. This will create some flow in the beaker, which will help get the mask of the sample.
4. Now take the sample and place it into the other beaker to prevent any residue floating onto the sample and place the beaker with the sample into a sonicator and let it sonicate for about 10 seconds at power 2-3. Too high power will remove the material that was just deposited. After sonicating spin dry the sample for 30 seconds at [amount] rpm.
5. Now the sample can be looked at under the optical microscope and see if there is any material left in unwanted areas. If so then repeat the process until the material is gone or the material will not go away at all.

Appendix B

Matlab code

All the measurements are processed by the program *data_process*, which averages all the data points from multiple traces and retraces to reduce the effect of noise. The program is run by *data_script* where the measurement parameters are given. All the residuals from the plots are made by programs *Datafit1w* & *Datafit2w* which use the standard matlab fit functions with given parameters, the parameters used can vary per dataset.

The SW model is applied by usin the program *AdjustedAngle*. What the program does is make the plot as shown in figure 2.10 then it will take the x (ψ) and y (θ) values used to make the plot. These values are then interpolated to have more datapoints. Then the angles of the real data are compared with the x values, which are both the angle of the magnetic field wrt the sample, and then be replaced by the y value corresponding to the x values or replaced by the angle of the magnetization

```
close all
A = importdata('data_27.dat');
X = A.data;
n = 360;
H_f = 350;
H_s = 175;
r = 1.05; %factor by which the value may differ
% [D, C, xdata, ydata, angleAdj] = data_process(X, n, H_f, H_s, r);
[D, C, xdata, ydata, angleAdj, xresi, yresi] = data_process(X, n, H_f, H_s, r, 1)
    ;
% A = importdata('data_25.dat');
% X = A.data;
% [D, C, xdata, ydata, angleAdj, xresi, yresi] = data_process(X, n, H_f, H_s, r,
    2);
% xl =  [56.7/12.5E-6, 49.99/12.5E-6, 30.44/12.5E-6]
% yl = [500 600 1000]
% xl =  [5.524E-3/12.5E-6, 4.833E-3/12.5E-6, 2.651E-3/12.5E-6]
```

```
%function for processing data
%X is input data set
```

```
%n - number of points measured

function [D, C, xdata, ydata, angleAdj, xresi, yresi] = data_process(X, n, H_f,
    H_s, r, kl)
[p, q]=size(X);
a = input('What data do you want to plot? (3=lockin1X, 4=1x processed, 5=lockin1Y
    , 6=1Y processed, 7-10 for 2X etc.)');
b = input('Include fit from curve tool? (1 for manual, 2 for automatic(not
    accurate))');
k=zeros(n);
l=0;
m =floor(p/n);
%m = 1;
B = zeros(floor(p/n),n);
E = zeros(floor(p/n),n);
% E1 = zeros(floor(p/n),n);
% E2= zeros(floor(p/n),n);
for i =1:n;
    for j=1:m;
       % if i+n*(j-1) > p
       %     break
       % end
        if mod(j,2)==0;
            B(j,i)=X(i+n*(j-1),1);
        else
            B(j,i)=X(n+1-i+n*(j-1),1);
        end
        if j > 1 && B(j,i) > r*B(j-1,i)
            B(j,i) = B(j-1,i);
        end
        l = l+1;
    end
    C(i,1)=sum(B(:,i))/l*pi/180;
    l=0;
end
% angleAdj = C'; xdata = 0; ydata = 0;
[xdata, ydata] = AdjustedAngle(H_f, H_s, 'C');
for i=1:n;
    [c index] = min(abs(C(i,1)-xdata));
    angleAdj(i) = ydata(index);
end
for i =1:n;
    for j=1:m;
        if mod(j,2)==0;
            E(j,i)=X(i+n*(j-1),a);
        else
            E(j,i)=X(n+1-i+n*(j-1),a);
        end
        if j ==1 && E(j,i)
        elseif j > 1 && E(j,i) > r*E(j-1,i)
            E(j,i) = E(j-1,i);
        end
        l = l+1;
    end
    D(i,1) = sum(E(:,i))/l;
```

```
%      D1(i,1)=sum(E1(:,i))/l;
%      D2(i,1)=sum(E2(:,i))/l;
     l=0;
end
% angleAdj(1:80) = []; D(1:80) = []; C(1:80) = [];
if a == 9||a == 10;
     figure(1)
     plot(angleAdj', D)
%      subplot(2,1,kl)
%      plot(angleAdj',D1)
%      hold on
%      plot(angleAdj',D2)
%      xlabel ('Magnetic field (T)')
%      ylabel ('R^{2w}(V/A^{2})')
     if b == 1
         [fitresult, gof] = localFit2w(angleAdj, D);
     end
elseif a==7||a==8
     figure(1)
     plot(angleAdj',D)
     if b == 1
         [fitresult, gof] = localFit2w(angleAdj, D);
     end
elseif a==5||a==6
     figure(1)
     plot(angleAdj',D)
elseif a==3||a==4
     figure(1)
     plot(angleAdj', D)
%      subplot(2,1,kl)
%      plot(angleAdj',D1)
%      hold on
%      plot(angleAdj',D2)
%      xlabel ('Magnetic field (T)')
%      ylabel ('R^{2w}(V/A^{2})')
     if b == 1
         [fitresult, gof, xresi, yresi] = data27Fit1walt(angleAdj, D);
     end
end
if b == 2
     for i = 1:9
              sinus = sprintf('sin%d',i);
              figure(2)
              f = fit(angleAdj',D,sinus);
              subplot(3,3,i)
              plot(f,angleAdj',D,'Residuals')
              title(sprintf('Residual of %d sine functions used to fit',i))
     end
end
% D = 0;
if b == 0;
     xresi = C;
     yresi = D;
end
% figure(4)
```

```
% subplot(3,3,i)
% plot(f)
% title(sprintf('%d th sine functions used to fit',i))

end
```

```
function [xnew, ynew] = AdjustedAngle(MagField, Saturization, x)
syms y;
eqn = 0.5*sin(2*y)==MagField/Saturization*sin(x-y);
figure(10)
eh = ezplot(eqn);
legend('psi vs. theta', 'Location', 'NorthEast' );
% Label axes
xlabel ('Angle of H wrt sample (theta)(rad)')
ylabel ('Angle of M wrt to sample (psi)(rad)')
grid on
xdata = eh.ContourMatrix(1,2:501);%for mostly linear (y=x) plots
ydata = eh.ContourMatrix(2,2:501);%for mostly linear (y=x) plots
%if plot is not (y=x) then the xdata and ydata need to be constructed
%manually once
set(groot,'defaultAxesColorOrder',[0 0 1;0 1 0;0 0 1],...
      'defaultAxesLineStyleOrder','-|--|:')
xnew=interp1(xdata,1:(499/(360*10-1)):numel(xdata));%chosen to be 10 times bigger
     than the measurement dataset
ynew=interp1(ydata,1:(499/(360*10-1)):numel(ydata));%chosen to be 10 times bigger
     than the measurement dataset
figure(1)
plot(xnew,ynew)
%h = gcf; %current figure handle
%axesObjs = get(h, 'Children');
%dataObjs = get(axesObjs, 'Children');
%objTypes = get(dataObjs, 'Type');
%xdata = get(dataObjs, 'Xdata');
%ydata = get(dataObjs, 'Ydata');
%zdata = get(dataObjs, 'Zdata');
end
```

```
function [fitresult, gof, xresi, yresi] = data27Fit1w(angleAdj, D)
%CREATEFIT(ANGLEADJ,D)
%  Create a fit.
%
%  Data for 'untitled fit 1' fit:
%      X Input : angleAdj
%      Y Output: D
%  Output:
%      fitresult : a fit object representing the fit.
%      gof : structure with goodness-of fit info.
%
%  See also FIT, CFIT, SFIT.

%  Auto-generated by MATLAB on 13-May-2016 16:16:59


%% Fit: 'untitled fit 1'.
[xData, yData] = prepareCurveData( angleAdj, D );
```

```
19
20 % Set up fittype and options.
21 ft = fittype( 'a*sin((x+c)/b)+d', 'independent', 'x', 'dependent', 'y' );
22 opts = fitoptions( 'Method', 'NonlinearLeastSquares' );
23 opts.Display = 'Off';
24 opts.Robust = 'Bisquare';
25 opts.StartPoint = [0.0025 0.5 0.7655 0.795199901137063];
26
27 % Fit model to data.
28 [fitresult, gof] = fit( xData, yData, ft, opts )
29
30 % Create a figure for the plots.
31 figure( 'Name', '45 degree out of plane first harmonic' );
32
33 % Plot fit with data.
34 subplot( 2, 2, 1 );
35 h = plot( fitresult, xData, yData );
36 legend( h, 'R^{1w}(Ohm) vs. Angle (rad)', 'fit', 'Location', 'NorthEast' );
37 % Label axes
38 xlabel ('Angle (rad)')
39 ylabel ('R^{1w}(Ohm)')
40 grid on
41
42 % Plot residuals.
43 figure(3);
44 h = plot( fitresult, xData, yData, 'residuals' );
45 legend( h, 'untitled fit 1 - residuals', 'Zero Line', 'Location', 'NorthEast' );
46 % Label axes
47 xlabel angleAdj
48 ylabel D
49 grid on
50
51 h = findobj(gca,'type','line');
52 xresi = h(2,1).XData;
53 yresi = h(2,1).YData;
54 %xresi=interp1(xdata,1:(499/(360*10-1)):numel(xdata));%chosen to be 10 times
       bigger than the measurement dataset
55 %yresi=interp1(ydata,1:(499/(360*10-1)):numel(ydata));%chosen to be 10 times
       bigger than the measurement dataset
56
57 %% Fit: 'untitled fit 1'.
58 [xData, yData] = prepareCurveData( xresi, yresi );
59
60 % Set up fittype and options.
61 ft = fittype( 'sin1' );
62 opts = fitoptions( 'Method', 'NonlinearLeastSquares' );
63 opts.Display = 'Off';
64 opts.Lower = [-Inf 0 -Inf];
65 opts.StartPoint = [0.000392386560968527 1.1*3.73990445985865 0.75];
66
67 % Fit model to data.
68 [fitresult, gof] = fit( xData, yData, ft, opts )
69
70 % Create a figure for the plots.
71 %figure( 'Name', 'untitled fit 1' );
```

```
72 figure(2);
73 % Plot fit with data.
74 subplot( 2, 2, 2 );
75 h = plot( fitresult, xData, yData );
76 legend( h, 'R^{1w}(Ohm) vs. Angle (rad)', 'fit', 'Location', 'NorthEast' );
77 % Label axes
78 xlabel ('Angle (rad)')
79 ylabel ('R^{1w}(Ohm)')
80 grid on
81
82 % Plot residuals.
83 figure(3);
84 h = plot( fitresult, xData, yData, 'residuals' );
85 legend( h, 'untitled fit 1 - residuals', 'Zero Line', 'Location', 'NorthEast' );
86 % Label axes
87 xlabel xresi
88 ylabel yresi
89 grid on
90
91 h = findobj(gca,'type','line');
92 xresi = h(2,1).XData;
93 yresi = h(2,1).YData;
94 %xresi=interp1(xdata,1:(499/(360*10-1)):numel(xdata));%chosen to be 10 times
       bigger than the measurement dataset
95 %yresi=interp1(ydata,1:(499/(360*10-1)):numel(ydata));%chosen to be 10 times
       bigger than the m
96
97
98 %% Fit: 'untitled fit 1'.
99 [xData, yData] = prepareCurveData( xresi, yresi );
100
101 % Set up fittype and options.
102 ft = fittype( 'sin1' );
103 opts = fitoptions( 'Method', 'NonlinearLeastSquares' );
104 opts.Display = 'Off';
105 opts.Lower = [-Inf 0 -Inf];
106 opts.StartPoint = [0.000242239512364485 6 1.79556634724802];
107
108 % Fit model to data.
109 [fitresult, gof] = fit( xData, yData, ft, opts )
110
111 % Create a figure for the plots.
112 figure(2);
113
114 % Plot fit with data.
115 subplot( 2, 2, 3 );
116 h = plot( fitresult, xData, yData );
117 legend( h, 'R^{1w}(Ohm) vs. Angle (rad)', 'fit', 'Location', 'NorthEast' );
118 % Label axes
119 xlabel ('Angle (rad)')
120 ylabel ('R^{1w}(Ohm)')
121 grid on
122
123 % Plot residuals.
124 figure(3);
```

```
125 h = plot( fitresult, xData, yData, 'residuals' );
126 legend( h, 'R^{1w} vs. Angle (rad)', 'fit', 'Location', 'NorthEast' );
127 % Label axes
128 xlabel ('Angle (rad)')
129 ylabel ('R^{1w}')
130 grid on
131
132 h = findobj(gca,'type','line');
133 xresi = h(2,1).XData;
134 yresi = h(2,1).YData;
135
136 %% Fit: 'untitled fit 1'.
137 [xData, yData] = prepareCurveData( xresi, yresi );
138
139 % Set up fittype and options.
140 ft = fittype( 'sin1' );
141 opts = fitoptions( 'Method', 'NonlinearLeastSquares' );
142 opts.Display = 'Off';
143 opts.Lower = [-Inf 0 -Inf];
144 opts.StartPoint = [0.000245253692045473 8 1.82366636175505];
145
146 % Fit model to data.
147 [fitresult, gof] = fit( xData, yData, ft, opts )
148
149 % Plot fit with data.
150 figure(2);
151 subplot( 2, 2, 4 );
152 h = plot( fitresult, xData, yData );
153 legend( h, 'R^{1w}(Ohm) vs. Angle (rad)', 'fit', 'Location', 'NorthEast' );
154 % Label axes
155 xlabel ('Angle (rad)')
156 ylabel ('R^{1w}(Ohm)')
157 grid on
158 return
```

```
1  function [fitresult, gof, xresi, yresi] = data27Fit2w(angleAdj, D)
2  %CREATEFIT(ANGLEADJ,D)
3  %  Create a fit.
4  %
5  %  Data for 'untitled fit 3' fit:
6  %      X Input : angleAdj
7  %      Y Output: D
8  %  Output:
9  %      fitresult : a fit object representing the fit.
10 %      gof : structure with goodness-of fit info.
11 %
12 %  See also FIT, CFIT, SFIT.
13
14 %  Auto-generated by MATLAB on 15-May-2016 16:33:46
15
16
17 %% Fit: 'untitled fit 3'.
18 [xData, yData] = prepareCurveData( angleAdj, D );
19
20 % Set up fittype and options.
```

```
21 ft = fittype( 'a*sin((x+c)/b)+d', 'independent', 'x', 'dependent', 'y' );
22 opts = fitoptions( 'Method', 'NonlinearLeastSquares' );
23 opts.Display = 'Off';
24 opts.Robust = 'Bisquare';
25 opts.StartPoint = [29 1 -1.45692520213929 -15];
26
27 % Fit model to data.
28 [fitresult, gof] = fit( xData, yData, ft, opts )
29
30 % Create a figure for the plots.
31 figure( 'Name', '90 degree out of plane second harmonic' );
32
33 % Plot fit with data.
34 subplot( 2, 2, 1 );
35 h = plot( fitresult, xData, yData );
36 legend( h, 'R^{2w}(V/A^{2}) vs. Angle (rad)', 'fit', 'Location', 'NorthEast' );
37 % Label axes
38 xlabel ('Angle (rad)')
39 ylabel ('R^{2w}(V/A^{2})')
40 grid on
41
42 % Plot residuals.
43 figure(3);
44 h = plot( fitresult, xData, yData, 'residuals' );
45 legend( h, 'untitled fit 3 - residuals', 'Zero Line', 'Location', 'NorthEast' );
46 % Label axes
47 xlabel angleAdj
48 ylabel D
49 grid on
50
51 h = findobj(gca,'type','line');
52 xresi = h(2,1).XData;
53 yresi = h(2,1).YData;
54
55 %% Fit: 'untitled fit 3'.
56 [xData, yData] = prepareCurveData( xresi, yresi );
57
58 % Set up fittype and options.
59 ft = fittype( 'sin1' );
60 opts = fitoptions( 'Method', 'NonlinearLeastSquares' );
61 opts.Display = 'Off';
62 opts.Lower = [-Inf 0 -Inf];
63 opts.StartPoint = [4 3 1.89207008846993];
64
65 % Fit model to data.
66 [fitresult, gof] = fit( xData, yData, ft, opts )
67
68 % Create a figure for the plots.
69 figure(2);
70
71 % Plot fit with data.
72 subplot( 2, 2, 2 );
73 h = plot( fitresult, xData, yData );
74 legend( h, 'R^{2w}(V/A^{2}) vs. Angle (rad)', 'fit', 'Location', 'NorthEast' );
75 % Label axes
```

```
xlabel ('Angle (rad)')
ylabel ('R^{2w}(V/A^{2})')
grid on

% Plot residuals.
figure(3);
h = plot( fitresult, xData, yData, 'residuals' );
legend( h, 'untitled fit 3 - residuals', 'Zero Line', 'Location', 'NorthEast' );
% Label axes
xlabel xresi
ylabel yresi
grid on

h = findobj(gca,'type','line');
xresi = h(2,1).XData;
yresi = h(2,1).YData;

%% Fit: 'untitled fit 3'.
[xData, yData] = prepareCurveData( xresi, yresi );

% Set up fittype and options.
ft = fittype( 'sin1' );
opts = fitoptions( 'Method', 'NonlinearLeastSquares' );
opts.Display = 'Off';
opts.Lower = [-Inf 0 -Inf];
opts.StartPoint = [1.80043160528997 5 -1.58933733156476];

% Fit model to data.
[fitresult, gof] = fit( xData, yData, ft, opts )

% Create a figure for the plots.
figure(2);

% Plot fit with data.
subplot( 2, 2, 3 );
h = plot( fitresult, xData, yData );
legend( h, 'R^{2w}(V/A^{2}) vs. Angle (rad)', 'fit', 'Location', 'NorthEast' );
% Label axes
xlabel ('Angle (rad)')
ylabel ('R^{2w}(V/A^{2})')
grid on

% Plot residuals.
figure(3);
h = plot( fitresult, xData, yData, 'residuals' );
legend( h, 'untitled fit 3 - residuals', 'Zero Line', 'Location', 'NorthEast' );
% Label axes
xlabel xresi
ylabel yresi
grid on

h = findobj(gca,'type','line');
xresi = h(2,1).XData;
yresi = h(2,1).YData;

```

```
131 %% Fit: 'untitled fit 3'.
132 [xData, yData] = prepareCurveData( xresi, yresi );
133
134 % Set up fittype and options.
135 ft = fittype( 'sin1' );
136 opts = fitoptions( 'Method', 'NonlinearLeastSquares' );
137 opts.Display = 'Off';
138 opts.Lower = [-Inf 0 -Inf];
139 opts.StartPoint = [1.803 7 -1.57248669787394];
140
141 % Fit model to data.
142 [fitresult, gof] = fit( xData, yData, ft, opts )
143 figure(2);
144 subplot(2,2,4);
145 % Plot fit with data.
146 h = plot( fitresult, xData, yData );
147 legend( h, 'R^{2w}(V/A^{2}) vs. Angle (rad)', 'fit', 'Location', 'NorthEast' );
148 % Label axes
149 xlabel ('Angle (rad)')
150 ylabel ('R^{2w}(V/A^{2})')
151 grid on
```

Bibliography

[1] LJ Cornelissen, J Liu, RA Duine, J Ben Youssef, and BJ Van Wees. Long-distance transport of magnon spin information in a magnetic insulator at room temperature. *Nature Physics*, 11(12):1022–1026, 2015.

[2] Vernor Vinge. The coming technological singularity: How to survive in the post-human era. 1993.

[3] Charles Kittel. *Introduction to solid state physics*. Wiley, 8th edition, 2005.

[4] Edwin H Hall. On a new action of the magnet on electric currents. *American Journal of Mathematics*, 2(3):287–292, 1879.

[5] Edwin Herbert Hall. Xviii. on the ¨rotational coefficient¨ in nickel and cobalt. *The London, Edinburgh, and Dublin Philosophical Magazine and Journal of Science*, 12 (74):157–172, 1881.

[6] AV Chumak, VI Vasyuchka, AA Serga, and B Hillebrands. Magnon spintronics. *Nature Physics*, 11(6):453–461, 2015.

[7] Felix Bloch. Zur theorie des ferromagnetismus. *Zeitschrift für Physik*, 61(3-4):206–219, 1930.

[8] Yaroslav Tserkovnyak, Arne Brataas, and Gerrit EW Bauer. Enhanced gilbert damping in thin ferromagnetic films. *Physical Review Letters*, 88(11):117601, 2002.

[9] Magnetic resonance. `http://www.larsenglish.com/magneticresonance`. Accessed: 06-06-2016.

[10] Vladimir Cherepanov, Igor Kolokolov, and Victor L'vov. The saga of yig: spectra, thermodynamics, interaction and relaxation of magnons in a complex magnet. *Physics reports*, 229(3):81–144, 1993.

[11] Nynke Vlietstra. *Spin transport and dynamics in magnetic insulator/metal systems*. PhD thesis, 2016.

[12] JE Hirsch. Spin hall effect. *Physical Review Letters*, 83(9):1834, 1999.

[13] Marvin L Goldberger and Kenneth M Watson. *Collision theory*. Courier Corporation, 2004.

[14] Luqiao Liu, Chi-Feng Pai, Y Li, HW Tseng, DC Ralph, and RA Buhrman. Spin-torque switching with the giant spin hall effect of tantalum. *Science*, 336(6081): 555–558, 2012.

[15] O Mosendz, JE Pearson, FY Fradin, GEW Bauer, SD Bader, and A Hoffmann. Quantifying spin hall angles from spin pumping: Experiments and theory. *Physical review letters*, 104(4):046601, 2010.

[16] Kazuya Ando, Saburo Takahashi, Junichi Ieda, Yosuke Kajiwara, Hiroyasu Nakayama, Tatsuro Yoshino, Kazuya Harii, Yasunori Fujikawa, M Matsuo, S Maekawa, et al. Inverse spin-hall effect induced by spin pumping in metallic system. *Journal of Applied Physics*, 109(10):103913, 2011.

[17] Michael Schreier, Gerrit EW Bauer, Vitaliy I Vasyuchka, Joost Flipse, Ken-ichi Uchida, Johannes Lotze, Viktor Lauer, Andrii V Chumak, Alexander A Serga, Shunsuke Daimon, et al. Sign of inverse spin hall voltages generated by ferromagnetic resonance and temperature gradients in yttrium iron garnet platinum bilayers. *Journal of Physics D: Applied Physics*, 48(2):025001, 2014.

[18] Jing Liu. Investigation of magnon transport in yttrium iron garnet using platinum and tantalum spin injection/detection electrodes, 2015.

[19] Y Onose, T Ideue, H Katsura, Y Shiomi, N Nagaosa, and Y Tokura. Observation of the magnon hall effect. *Science*, 329(5989):297–299, 2010.

[20] Onur Hosten and Paul Kwiat. Observation of the spin hall effect of light via weak measurements. *Science*, 319(5864):787–790, 2008.

[21] Yu Kagan and LA Maksimov. Anomalous hall effect for the phonon heat conductivity in paramagnetic dielectrics. *Physical review letters*, 100(14):145902, 2008.

[22] David J Griffiths and Edward G Harris. Introduction to quantum mechanics. *American Journal of Physics*, 63(8):767–768, 1995.

[23] Michael V Berry. Quantal phase factors accompanying adiabatic changes. In *Proceedings of the Royal Society of London A: Mathematical, Physical and Engineering Sciences*, volume 392, pages 45–57. The Royal Society, 1984.

[24] Naoto Nagaosa, Jairo Sinova, Shigeki Onoda, AH MacDonald, and NP Ong. Anomalous hall effect. *Reviews of modern physics*, 82(2):1539, 2010.

[25] DJ Thouless, Mahito Kohmoto, MP Nightingale, and M Den Nijs. Quantized hall conductance in a two-dimensional periodic potential. *Physical Review Letters*, 49 (6):405, 1982.

[26] FDM Haldane. Berry curvature on the fermi surface: Anomalous hall effect as a topological fermi-liquid property. *Physical review letters*, 93(20):206602, 2004.

[27] T Miyasato, N Abe, T Fujii, A Asamitsu, S Onoda, Y Onose, N Nagaosa, and Y Tokura. Crossover behavior of the anomalous hall effect and anomalous nernst effect in itinerant ferromagnets. *Physical review letters*, 99(8):086602, 2007.

[28] Shuichi Murakami. Berry curvature and topological phases for electrons, photons, and magnons. In *Proceedings of the International Symposium âœNanoscience and Quantum Physics 2012â(nanoPHYSâ^{TM}12)*, page 011001, 2015.

[29] KHAIRUL HABIB. *Thermal conductivity of thin films*. PhD thesis, 2005.

[30] K Uchida, S Takahashi, K Harii, J Ieda, W Koshibae, K Ando, S Maekawa, and E Saitoh. Observation of the spin seebeck effect. *Nature*, 455(7214):778–781, 2008.

[31] Edmund C Stoner and EP Wohlfarth. A mechanism of magnetic hysteresis in heterogeneous alloys. *Philosophical Transactions of the Royal Society of London A: Mathematical, Physical and Engineering Sciences*, 240(826):599–642, 1948.